NAG 5-740

IN-46

GRANT-CR

48304

P-78

Crustal Deformation in Great California Earthquake Cycles

by

Victor C. Li

Department of Civil Engineering
Massachusetts Institute of Technology
Cambridge, MA 02139

and

James R. Rice

Division of Applied Science
and Department of Earth and Planetary Sciences
Harvard University
Cambridge, MA 02138

October, 1986

SPONSORED BY
THE NATIONAL AERONAUTICS AND SPACE ADMININSTRATION,
THE NATIONAL SCIENCE FOUNDATION AND
THE UNITED STATES GEOLOGICAL SURVEY

(NASA-CR-180059) CRUSTAL DEFORMATION IN GREAT CALIFORNIA EARTHQUAKE CYCLES (Massachusetts Inst. of Tech.) 78 p
N87-15655
CSCL 08G
Unclas
G3/46 40247

Abstract

Periodic crustal deformation associated with repeated strike slip earthquakes is computed for the following model: A depth L ($\leq$H) extending downward from the Earth's surface at a transform boundary between uniform elastic lithospheric plates of thickness H is locked between earthquakes. It slips an amount consistent with remote plate velocity V_{pl} after each lapse of earthquake cycle time T_{cy}. Lower portions of the fault zone at the boundary slip continuously so as to maintain constant resistive shear stress. The plates are coupled at their base to a Maxwellian viscoelastic asthenosphere through which steady deep-seated mantle motions, compatible with plate velocity, are transmitted to the surface plates. The coupling is described approximately through a generalized Elsasser model. We argue that the model gives a more realistic physical description of tectonic loading, including the time dependence of deep slip and crustal stress build-up throughout the earthquake cycle, than do simpler kinematic models in which loading is represented as imposed uniform dislocation slip on the fault below the locked zone. Parameters of the model are chosen in accordance with seismic and geologic constraints and to fit the apparent time-dependence, throughout the earthquake cycle, of surface strain rates along presently locked traces of the 1857 and 1906 San Andreas ruptures. We find that prediction based on the resulting parameters compare reasonably to data on variations of contemporary surface strain and displacement rates as a function of distance from the 1857 and 1906 rupture traces, although the data is generally affected by asymmetry relative to the fault and by adjacent fault strands. Specifically, we fix V_{pl} = 35 mm/yr, T_{cy} = 160 yr and L = 9 to 11 km as a representative earthquake nucleation depth with a 2 km allowance for possible upward motion of the locked zone border during the earthquake cycle. We then find that the geodetic data is described reasonably, within the context of a model that is locally uniform along strike and symmetric about a single San Andreas fault strand, by lithosphere thickness H = 17 to 25 km and Elsasser relaxation time t_r = 10 to 16 yr. We conclude that the asthenosphere appropriate to describe crustal deformation on the earthquake cycle time scale lies in the lower crust and perhaps crust-mantle transition zone, and has an effective viscosity between about 2 x 10^{18} and 10^{19} Pa-s, depending on the thickness assigned to the asthenospheric layer.

Introduction

The northern part of the San Andreas fault in California was last broken by the great 1906 earthquake rupturing a 450 km segment. The southern part was broken last in 1857 with a rupture length of 350 km. Both of these fault segments have been locked since their last earthquake, with attendant strain accumulation over time. These locked segments are characterized by low levels of seismicity (see e.g., Carlson et al, 1979). In contrast, the San Andreas fault in central California appears to be creeping so that no long term strain accumulations occurs.

The nature of strain accumulation at a strike slip plate boundary has been discussed by various authors. In general, the strain rates are elevated near the fault and this is presumed to be due to deep aseismic slip or distributed shear flow along the downward continuation of the fault plane. The near surface fault locking and deep aseismic deformation is thought to be a result of material property contrasts. Near surface, the fault may generally be characterized as elastic and brittle. At greater depth, the material may be undergoing plastic shear flow due to the high temperature and pressure. Thus deformation would be expected to be aseismic and to accummulate continuously at depth while the upper crust has to accommodate relative movements between the North American Plate and the Pacific Plate by seismic faulting. Sibson (1982) and Meissner and Strehlau (1982) gave an account of the changing material properties with depth and explained the shallow confinement of seismicity on the San Andreas Fault in terms of a transition from brittle friction to ductile creep. Tse and Rice (1986) showed in an elaboration of this concept that the temperature and hence depth variation of fault slip constitutive properties, when incorporated into a mechanical model for plates joined at a transform boundary, led to predicted depth variable slip consistent with a shallow effectively locked zone that undergoes great seismic slips and with continuous slip accumulation below. Over the last several decades, strain changes have been monitored by geodetic networks at several locations along the fault. These data provide a basis for better understanding of the physical processes governing the behavior of the fault and, together with seismic and geologic data, are a source of possible constraints on locked zone depth, lithosophere thickness and rheological parameters.

Our goal here is to develop a simple physical model of the earthquake stressing process along the locked segments of the San Andreas fault that is compatible with such data. While we do not discuss here events leading to great earthquake instability, we expect that the improved description of the fault region geometry and rheological properties will be useful to more realistically representing the earthquake loading process in necessarily more complicated crustal scale instability models. Such models have been based on shear crack concepts (Dmowska and Li, 1982; Li and Rice, 1983; Tse et al., 1985; Li and Fares, 1986), fault surface slip-weakening response (Stuart and Mavko, 1979; Stuart, 1984/85; Stuart et al, 1985) or its generalization in the manner of slip rate and slip history dependent friction (Mavko, 1980; Tse and Rice, 1986).

Savage and Burford (1973) suggested the modelling of interseimic surface strain rate profiles near strike slip faults by means of a buried screw dislocation in an elastic half-space. The technique has been employed widely (e.g., Prescott et al., 1979; McGarr et al., 1982; Savage, 1983; King and Savage, 1984). In that approach there is assumed to be no slip at the transform margin within a presently locked seismogenic depth range, analogous to what we denote as L here, whereas a spatially uniform slip rate at the relative plate velocity V_{pl} is imposed at the margin everywhere along the downward continuation of the locked zone. Savage and Burford (1973) recognized this imposed motion on the plate boundary as a convenient simplification of a more complicated driving mechanism in which "the plates slip past one another in response to shear stresses that presumably orginate from the drag of mantle convection currents upon the bottom of lithospheric plates". Evidently, the motion at the transform margin below the locked zone would be a calculated response, rather than as imposed condition, in a more complete model of driving by deep-seated mantle motion and its coupling to the surface plates. While the modelling which we develop here is still severely simplified, it does nevertheless come closer to embodying the driving mechanism just described.

Turcotte and Spence (1974) analyzed the near-fault surface deformation by means of a two dimensional elastic edge crack model, like that in Fig. 1b. The crack faces represent the sliding portion of the plate margin and are assumed to slide under resistive shear stresses below the locked zone which remain uniform in time, with loading from the remote edges of the strip. Since the interest is in changes of displacement under ongoing loading, this constant stress condition is equivalent to treating the crack surfaces as freely slipping. Their analysis provided an appropriate assessment of the effect of the depth of locked zone on the profile of surface strain or displacement, particularly on the ratio between the near fault value to that at a point remote from the fault (where stress and strain alterations are presumably uniform through the thickness). The Turcotte-Spence crack model for the deeper fault zone, with its constant stress boundary condition, provides an alternative and presumably more realistic treatment of that zone than imposing a spatially uniform dislocation accumulating at a constant rate. That is, if the deeper fault zone deforms viscously with a strongly non-linear stress dependence as expected, then the local shear stresses will vary only modestly over appreciable changes in slip rate and are sensibly approximated as being uniform in time except in the co-seismic and short-term postseismic time intervals. Also, the resulting crack surface slip distribution tapers gradually to zero at the base of the locked zone, eliminating the unrealistic slip discontinuity of the uniform dislocation model.

Despite the attractive features of the crack model, its level of development by Turcotte and Spence remains of limited application because they assumed for simplicity in their modelling that the surface plates were decoupled from at least the nearby mantle below. Thus, they could only load the system by remotely applied forces and could not directly relate the loading to ongoing plate motion.

We remove these deficiencies so as to account approximately for the coupling of the lithosphere to a viscoelastic asthenosphere and to allow the overall lithosphere-asthenosphere system to be loaded by ongoing deep seated mantle motions that are compatible with remote plate velocities. As will be seen, this more complete analysis of the edge cracked model allows us to fit approximately the principal types of geodetic data now available, namely data on the time dependence of near fault deformation over the earthquake cycle and the variation of comtemporary deformation rates with distance from the fault trace.

The above mentioned works by Savage and Burford (1973) and followers, and by Turcotte and Spence(1974), being purely elastic, do not account for observed changes in strain rates over a complete earthquake cycle. Thatcher (1975) proposed a qualitative model for strain accumulation and release of the 1906 San Francisco Earthquake. Essentially, the fault was locked at the upper 10 km which was the focal depth. Tectonic plate movement drove the plate boundary deformation, which was localized along the fault due to aseismic sliding occurring below the locked zone. The accumulated strain was released by the 1906 earthquake, rupturing upwards through the locked portion. Post-seismically, the deeper part of the fault slid more rapidly, being driven by the stress shed onto it and the asthenosphere below by the earthquake. Thus, the postseismic surface strain rate was higher, but decreased gradually with time. For example, the (engineering) strain rate near the fault was about 2.4×10^{-6} yr^{-1} for the thirty years following the earthquake but was only 0.6×10^{-6} yr^{-1} since then (Thatcher, 1975). The time-dependence of crustal deformation near a fault may have two major sources: inelastic relaxation of the fault zone material below the seismogenic layer, and coupling between the elastic lithosphere and the viscoelastic asthenosphere. Thatcher (1983) modelled the aseismic deep slip by means of an elastic half space in which postseismic transient slip with exponential time decay is imposed kinematically as a spatially uniform dislocation. A Nur-Mavko model, in which an elastic layer is coupled to a viscoelastic half space is used to model the latter effect. This work provided important insight on the nonlinear nature of strain accumulation with time over an earthquake cycle. The strain rate data from northern and southern California (Thatcher, 1983) argues strongly in favor of this nonlinear accumulation. Our work here addresses the same data, but without the kinematic imposition of motion directly beneath the seismogenic zone. Rather, the deep fault walls move, in our modelling, in response to steady mantle motions, as transmitted through a viscoelastic asthenosphere, so as to maintain the constant resistive stress boundary condition. Turcotte et al (1984) addressed the time dependent straining with a multi-layer model, having an intracrustal as well as a deeper asthenosphere, that is somewhat in the spirit of the present approach, but did not include the strain concentrating effect of slip on deep fault walls within the elastic surface plate.

The Model

We build-in the viscoelastic asthenospheric coupling between the surface plate and deeper mantle motions by use of the 2-D generalized Elsasser model (Rice, 1980; Lehner et al, 1981). This results in a differential equation which is phrased in terms of thickness average stress and displacement. Further, to represent the edge cracked geometry with slipping crack walls at the plate margin, Fig. 1b, we require that the local displacement at the margin be related to the net shear force transmitted across it exactly as in the Turcotte-Spence analysis.

Thus, considering as in Fig. 1a, an elastic lithospheric plate underlain by a viscoelastic asthenosphere, for the strike slip environment of a long fault with uniform conditions along strike equilibrium requires that

$$\partial\sigma_{xy}/\partial y = \tau_x/H \tag{1}$$

Here $\sigma_{xy}(y,t)$ is the thickness average of the fault-parallel in-plane shear stress over plate thickness H and $\tau_x(y,t)$ is the fault-parallel shear stress draging on the base of the plate. For a homogeneous plate of shear modulus G, thickness averaging of the local stress-strain relation shows that

$$\sigma_{xy} = G\,\partial u/\partial y \tag{2}$$

where u(y,t) is the thickness average of the fault-parallel (and only nonvanishing) displacement.

The shear drag is connected to the displacement and displacement rate, within the approximate treatment of coupling in the model, through the linear Maxwellian relation

$$(b/G)\partial\tau_x/\partial t + (h/\eta)\tau_x = \partial u/\partial t - V_o(y) \quad (3)$$

which describes the deformation of the viscoelastic asthenosphere. In (3), b is a short-time effective elastic coupling thickness. It is chosen as $(\pi/4)^2H$ (Lehner et al, 1981) when G is the shear modulus of the elastic plate, in order for the final plate model to correctly respond to sudden stress release over the lithosphere thickness. Also, h/η is a long-time viscous compliance, interpretable as a depth scale h over which asthenospheric shear takes place divided by asthenospheric viscosity η. The velocity $V_o(y)$ is the rate of motion of sub-asthenospheric material of the mantle. It is assumed to be a function of y, but independent of t, such that $V_o(y) - V_o(-y)$ approaches the relative plate velocity V_{pl} as y increases. The function $V_o(y)$ represents the imposed steady driving motion although, as will be seen, the time dependence of deformation is remarkably independent of the detailed form of the function.

On combining (1), (2) and (3), the model requires that

$$(\alpha+\beta\,\partial/\partial t)\ \partial^2u/\partial y^2 = \partial u/\partial t - V_o(y) \quad (4)$$

where $\alpha \equiv HGh/\eta$ and $\beta \equiv bH \approx (\pi H/4)^2$. This is the equation governing the time and spatial distributions of deformation in the lithospheric plate, subject to a prescribed boundary condition at y = 0. (This boundary condition will be seen to be tied to V_{pl} and the earthquake cycle repeat time T_{cy}).

At the plate boundary, $y = 0^+$, the thickness average stress σ_{xy} transmitted is assumed to be related to the net thickness average displacement $2(u - D/2)$ through the stiffness k of the edge cracked structure with freely slipping crack walls (Figure 1b). Here D = D(t) represents the seismically accumulated slip of the presently locked shallow zone. The edge cracked structure in anti-plane strain may be regarded as a cross-sectional cut of the lithosphere at the plate boundary. For repeated earthquake cycles, D may be taken as a staircase function of time with periodic stepping, Fig. 2. Thus, the appropriate boundary condition for (4) at $y=0^+$ is

$$G\, \partial u/\partial y = 2k\, (u - D/2). \tag{5}$$

The stiffness k is given by (see eq. (8) to follow)

$$k = \pi G/4H \ \ln[1/\sin(\pi L/2H)]$$

where L is the locked depth. This is consistent with the stiffness k given by Tse et al. (1985) for "line spring" modelling of partially locked plate margins. An appropriate choice of L would be the focal depth of earthquake ruptures. For the extreme case of through thickness rupture, L is equal to H and the stiffness k goes to infinity. Equation (5) then implies u = D/2 which recovers the simple boundary condition used, in an earlier analysis by Lehner and Li (1982) of strain accumulation in the earthquake cycle.

To model periodic earthquakes with cycle time T_{cy} and slip magnitude D_1, the boundary slip D(t) may be decomposed into two parts, as shown in Figure 2. With the periodic saw-tooth function represented by a Fourier series, D(t) may be expressed as

$$D(t) = (D_1/\pi) \sum_{n=1}^{\infty} (1/n) \sin(2n\pi t/T_{cy}) + D_1 \, [(1/2) + t/T_{cy}] \tag{6}$$

In the steady state, it is assumed that the cumulative seismic slip agrees with the overall plate velocity V_{pl}. Thus, $D_1 = V_{pl}T_{cy}$. The second term of (6) may be understood as the value of 2u at $y = 0^+$ for a particular solution for u in $y>0$ of form $V_{pl}t/2$ + a function of y only, that reproduces the right hand side term $V_o(y)$ of (4). This solution has time rates representing steady rigid block motion and is otherwise of no interest in the present context. We are interested in the additional cyclically time dependent solution u to (4) with $V_o = 0$, in response to the first term of (6). The solution of (4) subject to (5) may be accomplished by means of separation of variables, and the detailed procedure is given in Appendix A. The solution to within the function of y just mentioned is

$$u(y,t) = (V_{pl}/2)\ (t + T_{cy}/2) \qquad (7)$$

$$+ V_{pl}t_r \sum_{n=1}^{\infty} (1/\omega_n B_n)\ \exp(-M_n Y)\ \sin(\omega_n t/t_r - \psi_n - N_n Y)$$

where $Y \equiv y/\sqrt{\beta} \approx 4y/\pi H$ and the terms B_n, ψ_n, M_n and N_n are functions of the circular frequencies $\omega_n \equiv 2\pi n t_r/T_{cy}$ and of a parameter λ (Appendix A) dependent on L/H. The Elsasser model relaxation time $t_r \equiv \beta/\alpha \approx (\pi^2 H/16h)(\eta/G)$ is essentially a fraction of the relaxation time for asthenosphere material; owing to the geometry of an elastic plate on a viscoelastic foundation, the time scale of lithosphere/asthenosphere coupling is appreciably longer (Rice, 1980; Lehner et al, 1981). All subsequent comparisons with data involve rates and hence are unaffected by the unwritten function of y.

The function u(y,t) as just calculated is the thickness averaged lithosphere displacement, and we must extract from it the displacement $u_s(y,t)$ at the Earth's surface. This is done as follows. Consider a plate as in Fig. 1b which has uniform shear modulus G and thickness H and has zero shear tractions on its base and on the vertical boundary below the locked ligament L. The plate is subjected to a remotely applied shear force σH, per unit distance along strike, and from solutions of the problem by Tada et al (1973), Turcotte and Spence (1974), and Tse et al (1985), this causes a uniform $\partial u/\partial y = \sigma/G$ everywhere except at $y = 0$, where u is discontinuous due to slip below the locked ligament (i.e., on $y = 0$, at depths $> L$), such that

$$u(y=0^{+}) = -u(y=0^{-}) = (2\sigma H/\pi G) \ln [1/\sin(\pi L/2H)] + D/2. \qquad (8)$$

The last term reflects that the now locked ligament has previously slipped by amount D. Thus, the thickness averaged displacement increases linearly with y for $y>0$ and $y<0$, but has a jump discontinuity at the fault trace, $y=0$. The surface displacement u_s mirrors this variation. Consider first the case $D = 0$. Then u_s too varies linearly with y, and is equal to u, at large $|y|$, but u_s is continuous at $y=0$. The jump discontinuity of u there is replaced by a continuous transition of u_s over a length scale determined primarily by L, but by H also. This variation is described by the function

$$S(y) = 1 - \frac{(\pi y/2H) - \ln\left[\sinh(\pi y/2H) + \sqrt{\sinh^{2}(\pi y/2H) + \sin^{2}(\pi L/2H)}\right]}{\ln[1/\sin(\pi L/2H)]} \qquad (9)$$

which can be extracted from the references above, and varies from $S=0$ at $y=0$ to $S=1$ at large y, such that (for $y>0$)

$$\begin{aligned} u_s(y) &= [u(y) - u(0^{+})] + u(0^{+})\, S(y) \qquad (10) \\ &= u(y) - u(0^{+})\, [1 - S(y)] \end{aligned}$$

When there is previous slip by amount D the equation remains correct if each u_s and u, for $y>0$, has subtracted from it a rigid motion D/2 so that there results

$$u_s(y) = D/2 + [u(y) - u(0^+)] + [u(0^+) - D/2]\ S(y). \qquad (11)$$

As examples, when $L = H/4$ one has $S(0) = 0$, $S(L) = 0.54$ and $S(H) = 0.96$, and when $L = H/2$, $S(0) = 0$, $S(L) = 0.72$ and $S(H) = 0.94$, illustrating the rapid approach to unity.

For the case when the lithospheric plate is coupled to a viscoelastic asthenosphere, we can use the foregoing analysis as a basis for estimating $u_s(y,t)$. That is, we assume as in the exact analysis reflected by eqs. (10, 11) above that u_s is essentially equal to u, except that the jump discontinuity in u at the fault trace shows up as a gradual variation in u_s spread out by the same function S(y). Thus we calculate u_s from

$$\begin{aligned} u_s(y,t) = D(t)/2 &+ [u(y,t) - u(0^+,t)] \\ &+ [u(0^+,t) - D(t)/2]\ S(y) \end{aligned} \qquad (12)$$

where D(t) is given as in Figure 2 and u(y,t), and thus $u(0^+,t)$, by the solution in eq. (7). Rates of fault parallel surface displacement and shear strain are then

$$\dot{u}_s = \partial u_s(y,t)/\partial t \quad , \quad \dot{\gamma}_s = \partial^2 u_s(y,t)/\partial y \partial t \qquad (13)$$

and these quantities are shown in various subsequent plots.

Since $u(0^+) - D/2$ is proportional, by eqs. (5) and (8), to the net force $\sigma(0)H$ transmitted across the locked ligament, eq. (12) expresses our assumption that it is this net force, together with geometric dimensions L and H as included in S(y), which determines the perturbation of the surface displacement and strain profile due to the freely slipping deep fault surface below.

For the present, we observe that the solution derived here has the form

$$\dot{u}_s(y,t) = (V_{pl}/2)\ F_1\ (y/H,\ t/T_{cy},\ L/H,\ t_r/T_{cy})$$

$$\dot{\gamma}_s(y,t) = (V_{pl}/H)\ F_2\ (y/H,\ t/T_{cy},\ L/H,\ t_r/T_{cy}) \qquad (14)$$

where F_1 and F_2 are universal dimensionless functions of their dimensionless arguments. Further as $y \rightarrow \infty$, $F_1 \rightarrow 1$ and $F_2 \rightarrow 0$. Also, F_1 is asymmetric and F_2 symmetric in y. These forms will enable interested readers to translate specific results given in later plots to some other sets of parameters.

The governing equation (4) of the deformation of the plate is based on the modified Elsasser model (Rice, 1980; Lehner et al, 1981). A characteristic of this plane stress model is in the use of thickness averaged quantities. Based on <u>through thickness</u> ruptures, Lehner and Li (1982) computed displacement profiles using the modified Elsasser approximations. Their results were compared with finite element calculations by Cohen and Kramer (1984), who suggested that the thickness averaging of parameters contributed a major source of inaccuracy in the prediction of the surface displacement field.

In the present model, the computed surface displacement (and subsequently the displacement rates and strain rates) takes into account the shallow locked depth $L<H$, which is embodied in the $S(y)$ terms in (10) - (12). We expect that the surface deformation field would then be most sensitive to the effect of continual shear below the locked ligament so that the above objection to the approach does not apply. We demonstrate that such is the case by considering (Appendix B) the extreme model of plates loaded at their base by uniform imposed displacements of opposite sign for $y>0$ and $y<0$, consistent with a uniform plate velocity V_{pl}. (This is a severe test since the base traction rates $\dot{\tau}_x$ are then localized near the fault trace, whereas our solutions show much broader loading zones (hence conditions more consistent with our use of the solution for the remotely loaded edge-cracked strip) well into the interseismic period; see the final figure in Appendix B.)

This boundary value problem has been solved exactly by conformal mapping techniques (Li and Lim, unpublished manuscript, 1986) and the relevant expressions for displacement rate and stress rate are given in Appendix B. For this model, eqn. (B3) and eqn. (B5) give the exact form of the surface displacement rate profile $\dot{u}_s(y)$ and the surface strain rate profile $\dot{\gamma}_s(y)$. If we now calculate for the base loading the associated thickness average quantities, eq. (12) and (13) then provide approximate estimates of the surface deformation consistent with our present procedure.

Comparisons of the exact $\dot{u}_s(y)$ and $\dot{\gamma}_s(y)$ with the approximate solutions, shown in Appendix B, reveal that the surface deformation fields calculated with (12) and (13) would be reasonably accurate in the case where the locked zone is shallow. We have made further comparisons between the exact and approximate models for the shear strain rates at the fault trace, and found that $\dot{\gamma}_{exact}/\dot{\gamma}_{approx} = 0.82 - 0.91$ for the locked zone depth and the lithosphere thickness of the best fit model for the San Andreas to be discussed shortly. This exercise demonstrates that the surface deformation field near the fault trace is more sensitive to the locked depth and the net driving load at the boundary than to the details of the coupling to the asthenospheric foundation. Thus, the approximations made in using thickness average displacement to estimate surface deformation by means of (12) and (13) is not expected to produce intolerable inaccuracy. (We assume that the model provides a reasonable account of time dependent force transmission at the margin and of thickness averaged displacement beyond the short term postseismic period). Note that Cohen & Kramer's comparison between their FE calculation and the modified Elsasser formulation is based on the full thickness rupture L = H analysis due to Lehner and Li, and is shown to be the worst case for the $\dot{\gamma}_{exact}/\dot{\gamma}_{approx}$ ratio. Further, the loading mode discussed provides a severe test of our procedures, which we know to become exact when base loads are instead applied remotely from the cracked section.

An unsatisfying aspect of the base loaded model shown in Fig. B1 is in the uniform imposed displacement (or velocity), implying a rigid foundation. This unrealistic feature, however, is overcome in the present Elsasser formulation.

It may be of interest to note that the lithosphere/asthenosphere coupling model of Savage and Prescott (1978) and its derivatives (Cohen and Kramer, 1984; Thatcher, 1983) is based on elastic plates overlying a viscoelastic half space in which the deformation in the shear zone below the seismogenic depth within the elastic plate is imposed kinematically as spatially uniform slip at a constant rate consistent with the remote plate velocity V_{pl}. This imposed uniform shear slip distribution, rather than one determined as here by coupling between the lithosphere and asthenosphere, strongly moderates the time-dependence of surface deformation. An implication is that for shallow faults, L<<H, coupling is predicted to be almost non-existent in their model since the near fault surface strain field would be almost completely controlled by the imposed dislocation rate. Indeed, Savage and Prescott (1978) reported that in their model, "the effect of asthenosphere relaxation is important only if the depth of the seismic zone is comparable to the thickness of the lithosphere". In contrast, the present model predicts response of the deep aseismic shear zone and it is found to respond in a spatially (in z) and time varying fashion as shown in Fig. 4 (see further explanation below).

Theoretical results, model parameters, and comparisons with time-dependent strain data from California

The complete surface strain rate at various fractions of an earthquake cycle is shown as a function of distance from the fault in Figure 3a,b. These figures compare results for two extremely different models, (a) locked through the entire depth H and (b) locked only over 0.3H. Immediately after the last rupture, the strain rate is high and localized near the fault due to rapid relaxation of the asthenosphere. It decays in amplitude and spreads spatially with increasing time. The rate of spreading is associated with the relaxation time of the asthenosphere. Observational support of such spreading of deformation is suggested by Thatcher (1983) on the basis of comparing the northern and southern sections of the San Andreas fault, and his composite estimate of strain rates at the fault trace for the two regions suggests decay in time. As expected, comparison between Figures 3a and 3b shows that a shallow locked segment tends to cause more localized deformation (at the fault) than one with most of the fault depth locked during the earthquake cycle.

To better understand the localized time-dependent straining at the fault, we recall that the relaxation of the asthenosphere causes a reloading of the plate boundary. This reloading causes a gradual shear flow of the fault zone at depths below the locked ligament. To illustrate, we show in Figure 4 the crack face slip (measured arbitrarily from zero immediately after an earthquake) at various fractions of a cycle time for the case in Fig. 3b. Note that the rate of slip as well as the surface strain rate slows down as the asthenosphere relaxes. For the case illustrated more than 70% of the total postseismic slip has occurred in the first half of the cycle. This is consistent with the post-seismic high strain rate shortly after the earthquake rupture as mentioned earlier.

We wish to make our description of the earthquake loading process, which (within the framework of the model adopted) means our choice of the five parameters V_{pl}, L, H, T_{cy} and t_r, consistent with seismic, geologic and geodetic evidence from the San Andreas fault region. Our approach is to choose V_{pl}, L and T_{cy} on the basis of geologic and seismic considerations and then to choose the less well constrained parameters H and t_r to fit the data set assembled by Thatcher (1983) for time dependent post-earthquake straining at a variety of locations along the San Andreas fault. Predictions based on the resulting parameter set are then compared to comtemporary fault-parallel displacement rates as a function of distance from the fault trace in a few places.

In the case of V_{pl}, it is accepted that the overall velocity between the Pacific and North American plates is approximately 55 mm/yr (Minster and Jordan, 1978). However, evidence from long term fault offsets summarized recently by Minster and Jordan (1984) and Stuart (1984/85), based on work by Sieh and Jahns (1984) and Weldon (1984), suggests that only 35 mm/yr should be regarded as taken up by the San Andreas fault, and we therefore set V_{pl}= 35 mm/yr.

In northern California great earthquakes like the 1906 rupture have been estimated to have a repeat time from 70 to more than 180 yr (Savage, 1983). A longer repeat time of 225 yr. based on trenching data was obtained by Hall et al. (1982). In southern California, data from extensive trenching at Pallet Creek (Sieh, 1984) leads to an average recurrence interval between 145 and 200 yr for large earthquakes, based on excavated evidence of 12 earthquakes between approximately 260 and 1857 A.D. Evidence from other locations along the 1857 rupture zone (Sieh and Jahns, 1984; Stuart 1984/85) suggests the possibility of a variable average recurrence interval from one segment to another, ranging from approximately 100 to 300 years. We have fixed T_{cy} = 160 yr, since this value is reasonable in terms of observations and since variations by ± 25% (expanding the range to 120 to 200 yr) have only very modest effects on the results which we show.

In terms of the model of a locked shallow portion of the crust with accumulating aseismic slip below, it seems logically consistent that the nucleation depth for a large earthquake should be identified with the highly stressed region at the border of the slipping and locked zones, i.e., with the crack tip location. This would argue for choosing L in the range of 8 to 10 km on the basis of seismically determined nucleation depths. For example, the 1979 Imperial Valley earthquake is inferred to have initiated at about 8 km depth (Archuletta, 1982), the 1966 Parkfield earthquake at about 9 km depth (Lindh and Boore, 1981), and both the 1979 Coyote Lake and 1984 Morgan Hill earthquakes along the Calaveras fault at about 10 km depth (Lee et al., 1979; Bouchon, 1982; Bakun et al., 1984). Also, Thatcher (1975) inferred a focal depth of not greater than about 10 km for the 1906 San Francisco earthquake based on analysis of geodetic data.

The nucleation depths discussed are towards the bottom of the seismogenic zone along the San Andreas, i.e., the zone extending typically to 12 to 14 km depth from which seismic signals emanate (Eaton et al., 1970; Wesson et al., 1973; Sibson, 1982).

In order to associate L with representative nucleation depths, we take L = 9 km as one case for more detailed study. However, in our present simplified modelling the locked zone depth L is regarded as fixed throughout the earthquake cycle. In reality, L will be time dependent if the slipping region gradually penetrates into the locked zone throughout the cycle. In that case the earthquake nucleation depth will underestimate a representative value of L for, say, mid-cycle straining conditions. We suggest that a choice of L = 11 km, which we take as a second case for detailed study, reasonably represents a locked zone depth in the presence of upward penetration.

As a first perspective on this choice, we note that the shear crack-like configuration implies that the locked region ahead of the crack tip is of mechanical properties such that it tends to resist deformation, but nevertheless ultimately breaks, in that it slips subsequently at reduced strength, when appropriate local stress levels are reached. Such properties define a deformation weakening material, i.e., a potentially brittle material, and are plausibly associated with material of the seismogenic zone. Thus the greatest plausible depth of locked zone would correspond to the 12 to 14 km base of the seismogenic zone; such would give the locked zone depth early in the cycle, whereas late in the cycle the depth has diminished to the 8 to 10 km nucleation depth range. These considerations suggest an upward motion of the locked zone on the order of 4 km throughout the earthquake cycle, and thus a mean depth around 10 to 12 km (we take L = 11 km), if indeed the locked zone depth does start off the cycle approximately coincident with the maximum seismogenic depth.

An independent but remarkably supportive perspective is provided by theoretical instability modelling. The shear crack and slip weakening instability models mentioned earlier all show a gradual upward penetration of the slipping zone. The recent work by Tse and Rice (1986) is perhaps the most realistic of that series in adopting a slip rate and slip history dependent form for the fault surface constitutive law based on laboratory experiments, and in using what (very incomplete) data is available on temperature and normal stress dependence of constitutive parameters, together with a San Andreas fault geotherm, to provide a depth variable description of material response. This (forward) modelling implied a transition from inherently stable to potentially unstable slip at around 11 km depth. Further, the results for slip histories throughout whole earthquake cycles calculated by Tse and Rice (1986) show clearly the development of a shallow locked zone which is gradually penetrated by slip below. Their simulations allowed for a broad range of critical slip weakening distances and different options for describing uncertainties of constitutive response; all were done with V_{pl} = 35 mm/yr and the resulting values for T_{cy} were between 50 and 160 yr. Examining simulations showing $T_{cy} > 80$ yr, one observes that the slipping zone below reached up to around 8 to 9 km depth when the deep slip reached 25% of $V_{pl}T_{cy}$ (i.e., 25% of its full cycle value), moved up to 7 to 8 km at 50% of $V_{pl}T_{cy}$, then to 6.5 to 7.5 km depth at 75% of $V_{pl}T_{cy}$, and to around 6 km just before instability. We may summarize by saying that the Tse-Rice modelling had an 11 km deep seismogenic zone and a locked depth at nucleation around 6 km (both a few km shallower than estimated above) and a locked zone depth around mid-cycle on the order 1 to 2 km deeper than that at instability, and 3 to 4 km shallower than the maximum seismogenic depth. These modelling results are not inconsistent with the simple description given above, and suggest that a representative locked zone depth at L = 11 km, 2 km below a typical nucleation depth, may account approximately for upward penetration. A feature not accounted for is that upward penetration would cause the strain near the fault trace to slightly increase even if the net force transmitted across the plate boundary were not increasing with time. This effect may act to slightly counteract the general trend of decreasing strain rate throughout the cycle that our present modelling implies.

For definiteness, we choose two cases L = 9 km and L = 11 km in what follows along with V_{pl} = 35 mm/yr and T_{cy} = 160 yr. There are no comparably good *apriori* constraints on the appropriate values of lithosphere thickness H and viscoelastic relaxation time t_r for purposes of describing the earthquake stressing process.

Thus as a general constraint on these model parameters for the San Andreas fault as a whole, Figure 5, we first compare the surface strain rate $\dot{\gamma}_s$ computed at the fault with Thatcher's (1983) compilation of data from Pt. Arena, Fort Ross, Pt. Reyes, Shelter Cove, S.F. Peninsula, Carrizo Plain, San Fernando-Mojave, Palmdale and Coachella Valley. Locations are shown in Figure 5, and Thatcher's plot of the data is shown in Figure 6 with his estimated error bars indicated. In reference to figure 6a, taking the locked zone as 9km, we found by a series of runs with different parameter values that a good fit to the data is given by t_r=12 yr and H=22.5km. The results of our calculation in that case are shown by the thick solid line, which we term our "reference" curve. To explain why fitting the data serves to constrain both t_r and H, we now examine the alteration to this reference case by varying one at a time. For the case of lowering the relaxation time to 6 yr, it is seen that the curve rotates by increasing the strain rate significantly at short time after the last rupture and drops below the reference curve approximately 20 years after the last rupture. While the short time prediction can arguably fit the geodetic data, the long time curve appears to underestimate the strain rate, lying below every data point except PR. As we shall see, the assumption of a thinner lithospheric thickness shifts the curve up at all times, and thus may help to improve the t_r=6 yr curve fit at long times, but would then aggravate the short time prediction. A similar analysis done for a much higher relaxation time of 18 yr. has the effect of rotating the curve downwards at short times and upwards at long time. While at short times, it passes through the error bars of the PA and FR points which may suggest a suitable fit, the long time prediction appears to over-estimate the strain rate data, with a clear exception of CP. One may again attempt to salvage this fit by using a larger H, which would indeed help in the long time, but would then aggravate the short time fit. The above attempts to study the effects of varying t_r suggests that t_r should be bounded by a lower limit of 6 yr. and an upper limit of

18 yr. The best fits appear to be in the range of 10 to 14 yr.

A study of the effect of varying the plate thickness from the reference value of 22.5km was also carried out. These results are also plotted in figure 6a and show an upper value of 30km (which puts the prediction on the low side compared to data) and a lower value of 15km (which puts the prediction on the high side). Again one may attempt to improve these fits by changing the relaxation time, but this always results in improving one part of the curve at the cost of making the other part much worse because of the rotating effect as discussed earlier. Thus the fitting of the data seems to constrain both t_r and H; significant alternations of one of the two from the value for our good fit reference curve cannot be compensated for by alteration of the other.

We have also analyzed the case for the locked zone L=11km. The results show a good fit with t_r=14km and H=20km, shown as the thick solid reference curve in figure 6b. In this figure we have also shown two fits of varying H up to 27.5km and down to 12.5, which somewhat bracket the data points. Again, we conclude that large variations of t_r or H from the reference values cannot give good fits for the reasons given in the previous paragraphs.

Since displacement rate profile predictions will be performed for various selected locations in this paper, it would be of interest to gain some insight into the influence of the model parameters on the predicted profiles. For this purpose, the same set of parameters used for the strain rate decay study in figure 6a was employed to compute the corresponding surface displacement rate profiles for a typical 'contemporary' time, t = 100 yr, and this result is shown in figure 7a. It shows that the displacement rate generally increases (in absolute values) with a higher relaxation time t_r and a smaller lithospheric thickness H, at least for this late (more than 60% of) cycle time. The variation of locked zone depth may also affect the displacement rate profiles, although the effect is ralatively small by varying L=6km to L=12km, as is shown in figure 7b.

Combination of eqs. (1) and (2) shows that the curvature $\partial^2\dot{u}/\partial y^2$ of a plot of $\dot{u}$ versus y is proportional to the rate of change $\dot{\tau}_x$ of mantle drag stress on the base of the plate. That is, it is proportional to the local rate of loading of the plate. The plots in Fig. 7 show $\dot{u}_s$ rather than $\dot{u}$ but the two are virtually indistinguishable for $y > H$. The fact that the plots in Fig. 7 still show appreciable curvature out to distances of order 3H (the plots all asymptote to a common level $V_{pl}/2 = 17.5$ mm/yr as $y \rightarrow \infty$) show that the region of base loading is very broad. This is in sharp distiction to the case discussed in Appendix B and, we argue, justifies our approximations embodied in eqs. (5) and (12) in analysis of the edge cracked strip.

Let us summarize as follows. If on the basis of typical rupture nucleation depths we assume the locked zone depth L = 9 km, and take V_{pl} = 35 mm/yr and T_{cy} = 160 yr, then the data of Fig. 6 on time dependent straining throughout the earthquake cycle is sensibly fit by assuming a lithosphere thickness H = 20 to 25 km and a relaxation time t_r = 10 to 14 yr. Substantial deviations of H and t_r from these ranges were shown to not allow acceptable fits to the data. Similarly, assuming L = 11 km to account approximately for the expected upward motion of the base of the locked zone during the cycle, i.e., an effective L greater than a typical nucleation depth, the data is sensibly fit by assuming H = 17 to 23 km and t_r = 12 to 16 yr.

Discussion: lithosphere thickness, possible crustal asthenosphere and relaxation time

It is useful to compare the inferred H and t_r values to some constraints obtained from other observations. This provides some confidence in our model predictions and sheds light on the larger tectonic implications of our results.

A wide range of lithosphere thickness values have been assumed in previous studies. Averages of oceanic and continental lithosphere thicknesses suggested by Stacey (1977) come to about 90 km, whereas Anderson (1975) used a 50 km oceanic lithosphere and Lehner et al. (1981) used a 75 km average lithosphere for generic illustration of viscoelastic coupling effects within the Elsasser framework. In a recent re-evaluation of isostatic rebound at Lake Bonneville, Nakiboglu and Lambeck (1983) used 28 to 30 km.

At the other extreme, and specifically for a lithospheric thickness along the San Andreas fault, Thatcher (1983) suggests that the elastic lithosphere may have a thickness of only 10 km. This was motivated by an attempt to rationalize the same data as in Figure 6, although our work here based on what we think to be a physically more valid model, without artifical kinematic imposition of deep fault slip, shows clearly that the data is compatible with much thicker values, 17 to 25 km. Further, Turcotte et al. (1984) pointed out that Thatcher's thin lithosphere would require a significantly higher heat flow than the relatively high value found over a broad region near the San Andreas fault, and they suggested a 30 km thick three layer lithosphere model which they coupled to the deeper surroundings by an Elsasser approximation. Their middle layer was intended to represent an intracrustal asthenosphere. However, a deficiency of their modelling is that they included no account of ongoing aseismic slip on the downward continuation of the locked seismic zone. Thus, while Turcotte et al. (1984) showed that they could choose parameters of their layer model to fit the sort of time-dependence of strain near the fault trace shown in Figure 6, we expect that in the absence of the strain concentrating effect of deep slip at the plate margin their model would not describe adequately the variation of surface strain or displacement rate with distance from the fault trace. They did not show results for what their model implied about such variations.

Finally, Tse et al (1985) have modelled geodetic data from the Parkfield region and adjacent central California creeping segment of the San Andreas fault by a model similar to what we examine here, involving elastic plates locked over part of the depth range at the plate margin, but freely slipping elsewhere. They assume a stress free base for the plates and thus load the system by remotely applied forces, as in the Turcotte and Spence (1974) crack modelling, but allow the geometry of the locked ligament to vary along strike and to not exist at all within the central region of the creeping zone. They show that the fit to data is better with H in the 30 to 40 km range than for larger values, but did not examine smaller values. Thus we can interpret their work as suggesting that H is less than approximately 40 km.

Evidently, the lithosphere thickness values of order 17 to 25 km that we infer are not incompatible with other studies. Further, these thicknesses are comparable to or less than representative crustal thicknesses, in that Oppenheimer and Eaton (1984) infer a Moho depth slightly above 24 km for the northern San Andreas between the PA (Point Arena) and CP (Carrizo Plain) symbols in Figure 5, with a thickening towards 26 km within approximately 50 km of those two points and a modest thinning towards 23 km at PR (Point Reyes). The tectonic significance of this observation is that the viscoelastic asthenosphere which enters our modelling must be presumed to correspond to the lower portions of the crust and perhaps a crust-mantle transition zone.

There may, of course, also exist beneath the San Andreas fault region a classical deep asthenosphere lying beneath a more elastic layer of upper mantle material, but we tentatively conclude that it is a lower crustal asthenosphere rather than that intra-mantle asthenosphere which contributes to time variations in the crustal deformation rate throughout the San Andreas earthquake cycle. We remark now and will return to the observation from Oppenheimer and Eaton (1984) that the crustal thickness decreases towards the ocean (i.e., southwest) side of the San Andreas fault, and increases toward the continental side. Near Point Reyes, this occurs at a steep rate of about 1.2 km change in crustal thickness per 10 km distance perpendicular to the fault (but they show thickness contour lines only on the continental side there and indicate that the uncertainties are greater than elsewhere), and more typically at a rate of 0.6 to 0.8 km change in crustal thickness per 10 km perpendicular distance. One infers, spurred on by some puzzling geodetic observations of Prescott and Yu (1986) to be discussed shortly, that to the ocean side of the San Andreas near Point Reyes, the already thin crust may possibly become too thin (hence too cool at its base) to sustain a crustal asthenospheric layer near its bottom.

An initially unexpected consequence of the inferred asthenosphere location in the lower crust is that the Elsasser type approximation for the viscoelastic coupling becomes yet more suitable since the relaxation would then seem to be confined to a relatively thin channel.

The relaxation time t_r is proportional to $H\eta/hG$, and there is considerable uncertainty associated with an *apriori* choice of a suitable asthenospheric viscosity η and depth scale h over which velocity gradients occur in viscous relaxation. Previous attempts to estimate η have generally assumed that the asthenosphere involved is of the classical intra-mantle type and are of uncertain relevance if a thin lower crustal asthenosphere is the correct picture. Nevertheless, with regard to η, Nur and Mavko (1974) inferred 5 x 10^{18} Pa-s from post seismic relaxation whereas Thatcher and Rundle (1979) and Thatcher et al (1980) suggested values of 4 x 10^{19} Pa-s and 1 x 10^{19} Pa-s, respectively, for post-seismic lithosphere rebound at underthrust zones. Walcott (1973) inferred 5 x 10^{19} Pa-s from isostatic rebound data at Lake Bonneville, and a recent reevaluation of that case by Nakiboglu and Lambeck (1983) suggested η = 1.5 to 3.4 x 10^{19} Pa-s when a 28 to 30 km elastic plate is assumed to lie over a uniform viscoelastic half-space, and 2.1 to 5.8 x 10^{18} Pa-s when the plate lies over a 100 km thick channel asthenosphere.

The crustal shear modulus near the San Andreas is G = 35 GPa, based on the average p-wave velocity of 6.0 km/sec (Oppenheimer and Eaton, 1984) and assuming a Poisson ratio of 0.25 and specific gravity of 2.9. Thus, the relaxation time t_r = 13 yr (middle of 10 to 16 yr range) implies η = 2.3 (h/H) x 10^{19} Pa-s. We have inferred that H = 17 to 25 km. Using H = 21 km and, since the asthenosphere is assumed to be confined to the lower crust and crust-mantle transition zone, assuming that h may range from 2 to 10 km, we conclude that viscosities of 2 x 10^{18} Pa-s to 10^{19} Pa-s are implied. These are in a range compatible with other estimates as just summarized. We have no independent check on their suitability or, indeed, on the adequacy of a linear characterization of viscoelastic response.

Contemporary fault parallel strain and displacement rates

Here we compare our model predictions, based on the parameters already chosen, to data other than that used to constrain the parameters. The data consists of geodetically measured contemporary fault parallel surface displacement rate profiles as a function of distance from the San Andreas fault, at three locations along the fault, and contemporary strain rates averaged over variable-sized areas at one location. Within the context of a model that involves uniform conditions along strike, and symmetry relative to the single fault strand representing the San Andreas in our surface plate, we believe that the comparison of prediction to data here is supportive of our model. Nevertheless, the displacement rate profiles at particular locations along strike, constructed from data for individual geodetic markers, are strongly affected by local conditions. Sometimes these suggest pronounced asymmetry of material properties or geometry relative to the San Andreas and show the effects of adjacent fault strands. Also, the data include features that suggest large non-uniformities along strike or, perhaps instead, inaccuracies relating either to marker instability relative to the crust below or to systematic measurement error. In one case, we note changes in model parameters which would improve the fit, but this is not always feasible within the symmetry of our model relative to the San Andreas fault.

Palmdale area (point PD in figure 5 and figure 8 and 9):

The displacement rate (average velocities, 1973-1983) data was deduced by King and Savage (1984) for 11 of the stations in Figure 8, from line length measurements using the "outer coordinate" solution method which minimizes the rms displacement normal to the San Andreas fault. Based on the line length changes, King and Savage concluded that there was no clear evidence of surface fault slip in the Tehachapi region. This data set has a relatively large scatter, and is plotted in figure 8 with the displacement rate zeroed on the San Andreas fault. The two theoretical curves shown are based on the parameters of the best fits to the strain rate decay data set shown in figure 6a and 6b.

They are computed at t = 123 yr (1857 + 123 = 1980), within the time period when the time measurements were made. Within the scatter of data, these parameters give apparently reasonable predictions to displacement rate profiles in the Palmdale area. The data is probably affected by the presence of the Garlock fault. King and Savage fit it with a buried screw dislocation model and conclude that a slightly better fit is obtained if they assume deep slip on the Garlock fault (at slightly less than half the rate they infer on the San Andreas), rather than slip on the San Andreas only. Their inferred locking depth is a poorly resolved 15 to 20 km, which we regard as questionable on seismic grounds and, in light of our results with much shallower locking depths, probably due to shortcomings of the buried dislocation model which we have discussed.

The strain rate averaged over various sub-nets of the network shown in Figure 8 (see figures 5 and 6 of King and Savage for locations of the sub-nets) was calculated by King and Savage (1984) and is listed in Table 1. Also listed is data for the Los Padres geodetic network, lying just to the NW of the region shown in Fig. 8 and mostly to the ocean side of the San Andreas (Savage, 1983), as summarized by McGarr et al. (1982). We have calculated the corresponding strain rate from our model using the same two sets of parameters mentioned earlier. The calculation was done based on the centroidal distance $\bar{y}$ of the net from the San Andreas fault (positive on continental side) and the root mean square distance $(\Delta y)_{rms}$ of the stations in the net, as given by McGarr et al. (1982), and these values are also given in Table 1. The strain rate calculations were based on a procedure attributed to Savage by McGarr et al., using

$$\dot{\gamma} = [\dot{u}_s(\bar{y} + (\Delta y)_{rms}) - \dot{u}_s(\bar{y} - (\Delta y)_{rms})]/2\ (\Delta y)_{rms} \qquad (15)$$

They implemented this formula with the buried screw dislocation model.

Our results based on our sets of reference parameters are tabulated as $\dot{\gamma}(a)$ for the L=9km case and $\dot{\gamma}(b)$ for the L=11km case. These calculated results are seen to be on the high side when compared to the observed strain rate. However, we have not attempted to fit this set of strain data, and the comparison can be improved by varying the model parameters. Owing to the uncertain effect of the Garlock fault, it is not clear that a fitting is justified. Nevertheless, Figures 7a and b show how slopes of the displacement rate profiles, i.e., the strain rates, can be altered by variation of L, H, and t_r, and, of course, the curves shown all have amplitude directly proportional to V_{pl}. We show as $\dot{\gamma}(c)$ in Table 1 the result which correspond to $V_{pl} = 32$ mm/yr, L = 9 km, H = 25 km, $t_r = 12$ yr, and $T_{cy} = 160$ yr just to emphasize that a good fit is possible with a locked depth that, we have argued, can be justified on seismological and material property considerations. In comparison, McGarr et al (1982) find that with the buried screw dislocation model the data implies a locked depth, again poorly constrained, around 22 km.

We may note also that the buried screw dislocation fits of King and Savage and McGarr et al. imply contemporary deep slip at rates of order 20 to 25 mm/yr. Our modelling shows that while points at the base of the surface plates, far removed from the fault trace, have relative motion at rates of $V_{pl} = 35$ mm/yr, the average contemporary slip rate on the freely slipping deeper portion of our fault zone, $2[H/(H-L)]\dot{u}(0^+,t)$, is only of order 4.9 to 6.4 mm/yr. The reason for this great difference will be evident from figures 3b, 4 and 7: at large times since the last earthquake the average deep slip rate diminishes considerably, but the accommodating region of the asthenosphere broadens out to several times the plate thickness.

Point Reyes area (point PR in Figure 5 and Figures 10 and 11):

Data for the period 1972-1982 from geodetic networks at Point Reyes (38.1°N), Santa Rosa (38.3°N) and Napa (38.0°N) was analyzed by Prescott and Yu (1986), updating data given previously by Prescott et al (1979). These networks are shown in Figure 10. Because of the proximity in latitude of the three mentioned locations, the displacement rate values from these networks provide a profile of fault parallel rate as a function of distance from the San Andreas. Figure 11 shows the component of surface displacement rate parallel to the fault trace, as compared to data assembled for all stations of each network by Prescott and Yu (1986). Their displacement data is analyzed as in Prescott (1981), in that a rigid body rotation has been chosen so as to mimimize displacements perpendicular to the fault trace. We have added a rigid translation to the data of Prescott and Yu (1986) so that zero fault-parallel displacement occurs at the San Andreas. The triangles are from the Geyser network to the north (Figure 10).

Our theoretical curves shown in Figure 11 with this data use the same sets of best fit parameters as deduced from the strain rate decay fit (figure 6a,b heavy solid curves). That is, the parameters are chosen independently of the Pt. Reyes area data set. The profiles are computed at t=73 yr. (1906+73=1979), within the time period when the line length measurements were made. The predicted profiles appear to match the observed displacement rates very well on the NE side of the fault up to distances beyond the Rogers Creek fault extending to y = 40 km. Beyond the West Napa fault, however, the data show clear deviation with higher rates than the predicted profiles. This may reflect accommodation of the part of the 55 mm/yr overall plate motion not attributable to the San Andreas. Similarly, while the predicted profiles match the two data points close and to the SW of the San Andreas, the other data points corresponding to the Point Reyes Head and Farallon Islands station velocities show marked deviation from an asymmetric displacement rate field about the San Andreas. We cannot judge the reliability of the data. As Prescott and Yu (1986) note, if valid, they suggest very much smaller shear strain rates to the SW of the fault than to the NE.

We have observed earlier that our relaxing asthenosphere is inferred, by fits to the strain rate decay data, to lie in the lower crust. Further, the seismically inferred crustal thickness by Oppenheimer and Eaton (1984) suggest that the crust is already slightly thinner near Point Reyes than elsewhere along the northern San Andreas fault and seems to be diminishing in thickness at an unusually high rate as one moves towards the fault from the NE side. Thus, the possibility arises that the crust becomes sufficiently thin on the SW side near Point Reyes that its (now shallow) lower regions are too cold to allow viscous relaxation. This line of argument suggests that the crustal asthenosphere may get pinched off to the SW side of the fault, so that the effective lithospheric thickness becomes much greater on that side and whatever deeper relaxation occurs there takes place in a classical sort of intra-mantle asthenosphere. This should result in a pronounced asymmetry of surface straining relative to the fault trace, but we do not yet know how to model it to compare against the data. Also, the discussion is speculative and driven by the two data points (Farallon Islands, Point Reyes Head) of uncertain significance. For example, aseismic undersea fault regions cannot be ruled out and could influence either data point.

Prescott and Yu (1986) develop an elaborate kinematical model to fit the data based on a distribution of buried screw dislocations in a half space. Their preferred distribution (model E in their paper) involves a pair of oppositely slipping screw dislocations at 6 and 10 km below the San Andreas, so as to accomplish spatially uniform slip at 10 mm/yr over the 6 to 10 km depth range, and to this they add an infinite number of infinitessimally slipping screw dislocations (i.e., a continuous distribution) at 10 km depth, spread out uniformly over the 50 km lateral distance from the San Andreas to the West Napa faults, so as to sum to 30 mm/yr total motion. In comparison, our theoretical predictions as shown in Fig. 11 suggest that the observed broad deformation profile between the San Andreas and West Napa fault may reasonably be interpreted as the result of ongoing mantle motion, together with laterally spreading viscoelastic asthenospheric relaxation from the great 1906 earthquake, taking place below an elastic plate of order 20 km depth. These features appear naturally in our physical (as opposed to kinematical) modelling, based on parameters chosen from other data sets.

Coachella Valley - Salton Sea Area (point CV in Figure 5 and Figures 12 and 13):

These networks cover a rather complicated area, with the San Jacinto fault and the Elsinore fault running parallel to the San Andreas fault, see Figure 12. These lines have been analyzed by Savage (1983), who obtained displacement rates (averaged over 1972-1981) as shown in Figure 13. The computed profiles are based on the same set of parameters which best fit the strain-rate decay data for the whole San Andreas fault (figure 6a, b). The profiles are calculated at 94% of cycle time, assuming the region has a relaxed foundation. However, the earthquake cycle time here is not known, although it is surely more than 160 yr. The fits are rather poor, as is perhaps attributable to the influence of the subparallel faults which essentially spread the plate boundary deformation over a much broader zone. Even if we focus only on the data points to the east of the San Andreas, the fits are still unsatisfactory. Clearly, a simple fault model with asymmetric displacement rates cannot adequately describe the surface deformation field in a region with active sub-parallel faults.

Conclusions

We have presented a physical model which allows the prediction of surface strain rates and surface displacement rates at a strike-slip plate boundary. The major features of this model are that it involves relatively thin elastic lithospheric plates (17 km to 25 km), locked between earthquakes over shallow depths (9 to 11 km) at the plate margin but with continuing aseismic slip below the locked zone, and that the surface plates are coupled by a Maxwell viscoelastic asthenosphere to upper mantle motions compatible with overall plate motions. The surface deformation is shown to be localized to the plate boundary (to within approximately three lithospheric plate thicknesses) due to deep aseismic slip below a locked brittle upper crust, modelled as stable shear sliding of crack faces at constant resistive stress in the anti-plane strain deformation of an edge cracked elastic strip.

The viscoelastic coupling is accomplished approximately by a generalized Elsasser model which provides the time-dependence of plate loading as well as the time dependence of the surface displacement and strain rates following sudden slips of the locked zone. Thus the complete earthquake cycle is modelled as sudden slip on the shallow locked upper crust (which will partially penetrate the aseismic shear zone) during an earthquake, which loads the asthenosphere. This is followed by the relaxation of the asthenosphere which reloads the surface plate, and this loading causes continuing aseismic slip below the now locked zone. Because of the relaxation effect of the asthenosphere, the stress accumulation and the surface deformation rates are non-linear in time over the earthquake cycle. Finally it should be emphasized that while the San Andreas fault may accomodate an overall slip rate of 35mm/yr, the contemporary slip rate below the locked zone may be much smaller than 35mm/yr. The substantially higher slip rate shortly after an earthquake rupture makes up the deficiency and produces an average rate of 35mm/yr over the earthquake cycle.

The essential parameters in the model are the plate velocity (that part of which is accomodated by the San Andreas fault), the locked zone depth, the surface plate thickness, the cycle time and the relaxation time of the modified Elsasser asthenospheric foundation. By arguments of previous geologic, geodetic and seismic studies, we have assumed the plate velocity to be 35mm/yr, the cycle time for the San Andreas as a whole to be 160yr, and the locked zone depth to be 9-11km. Thus the only free parameters in the model are the lithospheric plate thickness and the relaxation time of the foundation. The strain rate data from various locations of the San Andreas fault collected by Thatcher (1983) provides the constraints to these parameters, and it is found that the plate thickness cannot deviate significantly from 17km to 25km, while the relaxation time for the foundation cannot deviate significantly from 10yr to 16yr. We conclude that the asthenosphere appropriate to describe crustal deformation on the earthquake cycle time scale lies in the lower crust and perhaps in the crust-mantle transition zone and has an effective viscosity between about $2x10^{18}$ and 10^{19} Pa-s, depending on the thickness assigned to the asthenospheric layer.

To gain further insight into the nature of the contemporary distribution of surface deformation at the San Andreas fault, the model with parameters constrained as described above has been used to predict the surface displacement rate and surface strain rate profiles at several locations along the San Andreas where such data has been obtained from repeated geodetic line measurements. These include the geodetic net from the Palmdale area, from the Point Reyes area, and from the Coachella Valley-Salton sea area. The results indicate that good fits to data can be obtained, although the simple single fault geometry as contained in the present version of the model clearly cannot account for data contaminated by motions on branch faults or by material properties which are not distributed symmetrically about the San Andreas.

The model is seen here to fit the principal types of geodetic data now available along the San Andreas, consisting of strain rate near the fault trace as a function of time since the last great earthquake as assembled by Thatcher (1983), and of contemporary surface displacement rate as a function of distance from the fault trace. Thus, we conclude that such geodetic data does not require one to contemplate models involving an extremely thin elastic lithosphere that terminates just below seismogenic depths (Thatcher, 1983). While Turcotte et al (1984) were able to fit the San Andreas data of fig. 6 for $\dot{\gamma}_s$ as a function of time, using their four layer model, it is not yet clear whether their model also describes suitably the contemporary $\dot{\gamma}_s$ and $\dot{u}_s$ as a function of distance from the trace.

Even with its apparent successes, the model that we present here has evident limitations. For example, the aseismic shear zone at depth is assumed to creep-slip under constant resistive stress. However, in reality it may be expected that this zone supports larger stresses just after the earthquake in the shallow crust and then relaxes with time, hence producing a second source of time dependence which is not accounted for in the present model. It seems possible to incorporate this viscous shear effect of the deep aseismic shear zone approximately by modifying the boundary condition (5) from its present elastic relation between thickness average stress and slip to an appropriate viscoelastic relation. However, based on short term post-seismic deformation observation and modelling in subduction zones, Thatcher (1984) and Thatcher and Rundle (1984) suggested that the relaxation time for the deep shear zone is much shorter than for the asthenosphere, the former being on the order of a year or less and the latter tens of years. Hence, we may expect that our present results would not be affected by this modification if one is mainly concerned with long term interseismic plate boundary deformation and geodetic data interpretation, as we are in this paper. Also, there are simplifying approximations inherent in our use of the Elsasser foundation concept and Turcotte-Spence edge-cracked strip solution which could be improved upon in future work.

Appendix A: Solution of differential equation

We reproduce here the governing equation (4)

$$(\alpha + \beta\,\partial/\partial t)\ \partial^2u/\partial y^2 = \partial u/\partial t \tag{A1}$$

for the part of u that must respond to the first periodic sawtooth term in (6). This part is subject to the boundary condition (5)

$$G\ \partial u/\partial y = 2k(u - D/2) \qquad \text{on } y = 0 \tag{A2}$$

with D given by the sawtooth. Introducing the normalized parameters

$$Y \equiv y/\sqrt{\beta}, \qquad T \equiv \alpha t/\beta = t/t_r,$$
$$\lambda \equiv G/2k\sqrt{\beta} = (8/\pi^2)\ \ln\,[1 / \sin(\pi L/2H)]$$

(A1) and (A2) become

$$(1 + \partial/\partial T)\ \partial^2u/\partial Y^2 = \partial u/\partial T \tag{A3}$$

and

$$\lambda\ \partial u/\partial Y - u = -D/2 \qquad \text{on } Y = 0 \tag{A4}$$

We first look for the solution to the fundamental problem of a period slip function $D = D_o e^{i\omega T}$ and later superimpose all frequencies ω to form the complete solution to our problem. Let $u(Y,T) = u_o(Y)e^{i\omega T}$. Then (A3) and (A4) become

$$(1 + i\omega)\ \partial^2u_o/\partial Y^2 = i\omega u_o \tag{A5}$$

$$\lambda\ \partial u_o/\partial Y - u_o = -\ D_o/2 \qquad \text{on } Y = 0^+ \qquad \text{(A6)}$$

from which it may be shown that

$$u_o(Y) = [D_o/2B(\omega)]\ \exp\ \{-M(\omega)Y - i[N(\omega)Y + \psi(\omega)]\}$$

where

$$M(\omega) = \sqrt{\omega[\rho(\omega) + \omega]/2[\rho(\omega)]^2}$$

$$N(\omega) = \sqrt{\omega[\rho(\omega) - \omega]/2[\rho(\omega)]^2}$$

$$\rho(\omega) = \sqrt{1 + \omega^2}$$

$$B(\omega) = \sqrt{1 + 2\lambda M(\omega) + \lambda^2\omega/\rho(\omega)}$$

$$\psi(\omega) = \arctan\ \{\lambda\ N(\omega)/[1 + \lambda\ M(\omega)]\}$$

Hence, for $D(T) = \text{Im}\ (D_o e^{iwt}) = D_o \sin \omega T$,

$$u(Y,T) = [D_o/2B(\omega)]\ \exp\ [-M(\omega)Y]\ \sin\ [\omega T - N(\omega)Y - \psi(\omega)] \qquad \text{(A8)}$$

As the periodic sawtooth function may be represented by an infinite sine series, the solution for u(Y,T) also takes the form of a sine series, made up of fundamental solutions given by (A8) with the appropriate frequency ω. The complete form of u(Y,T) is given by equation (7). For numerical convergence, we have removed terms summing to known discontinuous functions of time (e.g., sawtooths) from within the summation signs. The actual expression used for numerical computation is given below for the thickness averaged displacement rate:

$$\frac{1}{V_{pl}}\frac{\partial u}{\partial t}(Y,t) = \frac{1}{2} + \frac{e^{-Y}}{1+\lambda}\left[\frac{1}{4}\left(\frac{1}{2}-\frac{t}{T_{cy}}\right)\left(\frac{\lambda}{1+\lambda}+Y\right)\frac{T_{cy}}{t_r}-\frac{1}{2}\right]$$

$$+\sum_{n=1}^{\infty}(\alpha_n \sin(\omega_n t/t_r) + \beta_n \cos(\omega_n t/t_r)] \tag{A9}$$

where

$$\alpha_n = \frac{e^{-M_nY}}{B_n}\sin(\psi_n + YN_n) - \frac{e^{-Y}}{1+\lambda}\left(\frac{1}{2\omega_n}\right)\left(\frac{\lambda}{1+\lambda}+Y\right)$$

$$\beta_n = \frac{e^{-M_nY}}{B_n}\cos(\psi_n + YN_n) - \frac{e^{-Y}}{1+\lambda}$$

$$\omega_n = 2\pi n t_r/T_{cy}$$

and where M_n, N_n, ρ_n, B_n, and ψ_n are the functions of ω given above evaluated at $\omega = \omega_n$.

Also, for thickness averaged shear strain rate, we use

$$\frac{H}{V_{pl}}\frac{\partial^2 u}{\partial y \partial t} = \frac{2}{\pi}\frac{e^{-Y}}{1+\lambda}\left[1+\frac{1}{2}\left(\frac{T_{cy}}{t_r}\right)\left(\frac{1}{1+\lambda}-Y\right)\left(\frac{1}{2}-\frac{t}{T_{cy}}\right)\right]$$

$$-\Omega\pi^2\left[(1/6) - (t/T_{cy}) + (t/T_{cy})^2\right] \tag{A10}$$

$$-\sum_{n=1}^{\infty}\left[\theta_n \sin(\omega_n t/t_r) + \gamma_n \cos(\omega_n t/t_r)\right]$$

where

$$\Omega = -\frac{1}{8\pi^3}\,\frac{e^{-Y}}{1+\lambda}\left(\frac{T_{cy}}{t_r}\right)^2\left[Y^2 - \left(\frac{5+3\lambda}{1+\lambda}\right)Y + \frac{3+\lambda}{(1+\lambda)^2}\right]$$

$$\theta_n = -\frac{4}{\pi B_n}\,e^{-M_nY}\left[N_n\cos(\psi_n+N_nY) - M_n\sin(\psi_n+N_nY)\right]$$

$$+\frac{2}{\pi\omega_n}\,\frac{e^{-Y}}{1+\lambda}\left(\frac{1}{1+\lambda} - Y\right)$$

$$\gamma_n = \frac{4}{\pi}\left[\frac{e^{-M_nY}}{B_n}\left[M_n\cos(\psi_n + N_nY) + N_n\,\sin(\psi_n + N_nY)\right] - \frac{e^{-Y}}{1+\lambda}\right] - \frac{\Omega}{\pi^2}$$

Notice that all the coefficients α_n, β_n, θ_n and γ_n of the sine and cosine terms in the summations vanish as $1/n^2$ as $n \to \infty$, which accelerates the series convergence. Equations (A9) and (A10) are the actual expressions used for numerical evaluation of equations (12) and (13).

Appendix B: Accuracy of surface displacement estimation by eqn. (12) and (13)

We consider the deformation of an elastic plate of thickness H with an edge crack of length a ($\equiv$H-L), loaded at the base of the plate by imposed displacement rate $V_{pl}/2$ for y>0 and $-V_{pl}/2$ for y<0, as shown in Fig. B1. This loading configuration represents an extreme case of lithosphere/asthenosphere coupling where the elastic lithosphere is driven by a rigid foundation moving at uniform velocity consistent with the far field plate motion. We shall call this the uniform base driven model.

For this extreme case, 2-D elasticity theory leads to a governing equation for the only non-vanishing displacement rate component w(y,z):

$$\nabla^2 w = 0 \qquad \text{(B1)}$$

subject to the boundary conditions indicated in Fig. B1.

The solution to this boundary value problem has been obtained by means of the conformal mapping technique and the details are reported elsewhere (Li and Lim, unpublished manuscript, 1986). Here we summarize the resulting expressions relevant to the present discussion:

(1) Displacement rate in Body:

$$w(y,z) = (V_{pl}/2)\ \mathrm{Re} \int_o^p \frac{dt}{\sqrt{F(1-t^2)(1-k^2t^2)}} \qquad \text{(B2)}$$

where $k = \sin\alpha$

$$F = \int_{o}^{\pi/2} \frac{d\theta}{\sqrt{1-k^2\sin^2\theta}}$$

is the elliptical integral of the 1st kind

$$p = \mathrm{Re}\sqrt{1 + \tanh^2(\gamma+i\beta)/\tan^2\alpha}$$

$$\alpha \equiv \pi a/2H; \quad \gamma \equiv \pi y/2H; \quad \beta \equiv \pi z/2H$$

(2) Surface displacement rate (at z=H)

$$\dot{u}_s(y) \equiv w(y,z=H) = V_{pl}/2 \left[1 - (1/F) \int_{1/k}^{\lambda} \frac{dt}{\sqrt{(t^2-1)(k^2t^2-1)}} \right] \tag{B3}$$

where $\lambda \equiv \sqrt{1 + \coth^2\gamma/\tan^2\alpha}$

(3) Stress rate in body:

$$\dot{\tau}_{yx} - i\,\dot{\tau}_{zx} = \frac{G(V_{pl}/2F)(\pi/2H)}{\sqrt{\sin[i\gamma - (\beta-\alpha)]\ \sin[i\gamma - (\beta+\alpha)]}} \tag{B4}$$

(4) Surface strain rate (at z=H)

$$\dot{\gamma}_s(y) = \frac{(V_{pl}/2F)(\pi/2H)}{\sqrt{\sinh^2\gamma + \cos^2\alpha}} \tag{B5}$$

We compare predictions of surface deformation rate from the exact solution, here called $\dot{u}_S^E(y)$, just obtained to that predicted from two versions of eq. (12) in the text:

$$\dot{u}_s^A(y) = \dot{u}(0^+)\ S(y) + [\dot{u}(y) - \dot{u}(0^+)] \tag{B6}$$

and

$$\dot{u}_s^B(y) = [\dot{\sigma}(0)/2k]\ S(y) + [\dot{u}(y) - \dot{u}(0^+)] \tag{B7}$$

where $\dot{u}(y)$ again denotes the thickness average of $w(y,z)$ and $\dot{\sigma}(y)$ is the thickness average of $\dot{\tau}_{yx}(y,z)$. These comparisons, calculated for $L = 0.25H$, $0.5H$ and $0.75H$ are shown in figure B2. In equation (B6) and (B7), $\dot{u}$ and $\dot{\sigma}$ are thickness averages of displacement and shear stress based on the exact solution and k is the stiffness of eq. (5). When the edge cracked strip is loaded by surface tractions that act remotely from the crack section, $\dot{\sigma}(0) = 2k\dot{u}(0^+)$ so that versions A and B are equivalent. In the present case, however, owing to the imposition of displacements directly at the bottom of the crack, we find that the crack slip profile deviates to larger values at depth from the profile expected from remotely applied loading, so that $\dot{u}(o^+)$ slightly exceeds $\dot{\sigma}(0)/2k$. Thus, $\dot{\sigma}(0)$ is numerically very close to $2k\dot{u}(0^+)$ only at small L/H. The latter version B then more successfully embodies the notion that the deformation perturbation at the fault trace is governed by the net force transmitted across the locked ligament. We do not replace the second $\dot{u}(0^+)$ in version B by $\dot{\sigma}(0)/2k$, since that would give a discontinuity to $u_s(y)$ at $y = 0$, equal to the difference $\dot{u}(0^+) - \dot{\sigma}(0)/2k$. (The predicted $\dot{u}_s^B(y)$ at $y = \infty$ in version B is, however, too small by the same difference). Note that the second $\dot{u}(0)$ makes no contribution whatever to the surface strain rate $\dot{\gamma}$ =

$d\dot{u}_S/dy$, so that $\dot{\gamma}$ in version B is determined entirely by the net force distribution, that is by the distribution $\dot{\sigma}(y) = G\, d\dot{u}(y)/dy$.

The estimated surface strain rate profile may be obtained from a direct differentiation of (B7) with respect to y:

$$\dot{\gamma}_s(y) = [\dot{\sigma}(O)/2k]\ \partial S(y)/\partial y + \partial\dot{u}(y)/\partial y \tag{B8}$$

This may be compared with the exact solution (B5) and the comparison is shown in Figure B3, for three different locked zone depths. Furthermore the ratio of the surface strain rate at the fault trace for the exact solution to that for the approximate solution B is shown in Fig. B4, as a function of locked zone depth.

The surface displacement and strain rates for the edge-cracked strip can be regarded as the response of an elastic body to the base loading rate $\dot{\tau}_x$. The heavy solid curve in Figure B5 shows the distribution of loading rate for the base driven model discussed in this appendix, when $L/H = 0.5$. The loading rate is concentrated near the fault zone and thus introduces the moderate errors shown in figures B2 to B4. The loading rate distributions at various fractions of the cycle time are also shown in figure B5 for the model as developed in the text, using $t_r/T_{cy} = 12\ \mathrm{yr}/160\mathrm{yr} = 0.075$. Evidently, those loading rates has, by comparison, a very broad distribution at mid- and late-cycle times creating base loading conditions that are more compatible with the approximations in our modelling procedures.

Acknowledgements

The authors wish to thank H.S. Lim for making computational runs in the preparation of this manuscript, and to acknowledge comments on an earlier version of this manuscript by N.E. King, W. Thatcher and unidentified reviewers which contributed to the improvement of the paper. The manuscript has been typed by M. Weir. V.C.L. was supported at the start of this work by grants from NSF and USGS to M.I.T. and, for the completion of the work, by a NASA grant to M.I.T.; J.R.R. was supported throughout by NSF and USGS grants to Harvard.

References

Allen, C. R., The tectonic environments of seismically active and inactive areas along the San Andreas fault system. Proceedings, Conference on Geologic Problems of San Andreas Fault System (eds. W. R. Dickinson & A. Grantz), Stanford Univ. Publ., Geol. Sci. Vol. 11, 70-82, 1968.

Anderson, D. L., Accelerated plate tectonics, Science, 187, 1077-1079, 1975.

Archuletta, R. J., Hypocenter for the 1979 Imperial Valley Earthquake, Geophys. Res. Letters, 9, 625-628, 1982.

Bakun, W. H., M. M. Clark, R. S. Cockerham, W. L. Ellsworth, A. G. Lindh, W. H. Prescott, A. F. Shakal and P. Spudich, The 1984 Morgan Hill California earthquake, Science, 225, No. 4659, 288-291, 1984.

Bouchon, M., The rupture mechanism of the Coyote Lake earthquake of August 6, 1979 inferred from near field data, Bull. Seismol. Soc. Amer. 72, 745-758, 1982.

Carlson, R., H. Kanamori and K. McNally, A. Survey of microearthquake activity along the San Andreas fault from Carrizo Plain to Lake Hughes, Seismol. Soc. Amer. Bull., 69, 177-186, 1979.

Cohen, S. C. and M. J. Kramer, Crustal deformation, the earthquake cycle, and model of viscoelastic flow in the asthenosphere, Geophys. J. R. Astr. Soc., 78, 735-750, 1984.

Eaton, J. P., M. E. O'Neill and J. N. Murdock, Aftershocks of the 1966 Parkfield-Cholame, California earthquake: a detailed study Bull. Seism. Soc. Am. 60, 1151-1197, 1970.

Ellsworth, W. L., A. G., Lindh, W. H. Prescott and D. G. Herd, The 1906 San Francisco earthquake and the seismic cycle, in Earthquake Prediction, An International Review, Maurice Ewing Ser., Vol. 4, ed. D. W. Simpson and P. G. Richards, 126-140, AGU, Washington, D.C., 1981.

Hall, N. T., E. A. Nelson, D. R. Fowler, Holocene activity on the San Andreas Fault between Crustal Springs Reservoir and San Andreas Dam, San Mateo Country, Calif. Presented at Ann. Meet. Cordilleron Sect., Geol. Soc. Am., 78th, Anaheim, Calif., 1982.

Lee, W. H. K., D. G. Herd, V. Cognetti, W. H. Bakun and A. Raport, A preliminary study of the Coyote Lake earthquake of August 6, 1979 and its major aftershocks, U.S. Geological Survey, Open File Report 79-1621, 1979.

King, N. E. and J. C. Savage, Regional deformation near Palmdale, California, 1973-1983, J. Geophys. Res., 89, 2471-2477, 1984.

Lehner, F. K., V. C. Li and J. R. Rice, Stress diffusion along rupturing plate boundaries, J. Geophys. Res., 86: 6155-6169, 1981.

Lehner, F. K., V. C. Li, Large-scale characteristics of plate boundary deformations related to the post-seismic readjustment of a thin asthenosphere, Geophys. J. R. Astr. Soc. 71, 775-792, 1982.

Li, V. C. and N. Fares, Rupture processes in the presence of creep zones, Earthquakes Source Mechanics, Maurice Ewing 6, (ed. S. Das, J. Boatwright & C. H. Scholz), 71-80, 1986.

Li, V. C. and J. R. Rice, Preseismic rupture progressions and great earthquake instabilities at plate boundaries, J. Geophys. Res., 88: 4231-4246, 1983a.

Li, V. C. and J. R. Rice, Precursory surface deformation in great plate boundary earthquake sequences, Bull. Seism. Soc. America, 73, 1415-1434, 1983b.

Lindh, A. G. and D. M. Boore, Control of rupture by fault geometry during the 1966 Parkfield Earthquake, Bull. Seism. Soc. America, 71, 95-116, 1981.

Mavko, G. M., Simulation of earthquakes and creep events on a spatially variable model (Abstract), EOS, Trans AGU, 61, 1120, 1980.

McGarr, A., M. D. Zoback and T. C. Hanks, Implications of an elastic analysis of in-situ stress measurements near the San Andreas fault, J. Geophys. Res., 87, 7797-7806, 1982.

Meissner, R. and J. Strehlau, Limits of stress in continental crusts and their relation to the depth-frequency distribution of shallow earthquakes, Tectonics, 1, 73-89, 1982.

Minster, J. B. and T. H. Jordan, Vector constraints on quaternary deformation of the western United States east and west of the San Andreas Fault, in Tectonics and sedimentation along the California margin, ed. by J. K. Crouch and S. B. Bachman, Pacific Section S.E.P.M., Vol. 38, pp. 1-16, 1984.

Minster, J. B., T. H. Jordan, Present-day plate motions, J. Geophys. Res. 83, 5531-54, 1978.

Nakiboglu, S. M. and K. Lambeck, A reevaluation of the isostatic rebound of Lake Bonneville, J. Geophys. Res., 88, 10439-10448, 1983.

Nur, A. and G. Mavko, Post-seismic viscoelastic rebound, Science, 183, 204-206, 1974.

Oppenheimer, D. H. and J. P. Eaton, Moho orientation beneath central California from earthquake travel time, J. Geophys. Res., 86, 6067-6072, 1981.

Prescott, W. H., J. C. Savage, W.T. Kinoshita, Strain accumulation rates in the western United States between 1970 and 1978, J. Geophys. Res., 84: 5423-5435, 1979.

Prescott, W. H. and A. Nur, The accommodation of relative plate motion at depth on the San Andreas fault system in California, J. Geophys. Res., 86, 99-1004, 1981.

Prescott, W. H. and S. B. Yu, Geodetic measurement of horizontal deformation in the northern San Francisco Bay region, California, J. Geophys. Res., 91, 7475-7484, 1986.

Rice, J. R., The Mechanics of earthquake rupture, in Physics of the Earth's Interior, ed. by A. M. Dziewonski and E. Boschi, 555-649, Italian Physical Society/North Holland, Amsterdam, 1980.

Savage, J. C. and R. O. Burford, Geodetic determination of relative plate motion in Central California, J. Geophys. Res., 78, 832-845, 1973.

Savage, J. C., Strain accumulation in Western United States, Ann. Rev. Earth Planet, Sci. 11: 11-43, 1983.

Savage, J. C. and W. H. Prescott, Asthenosphere readjustment and the earthquake cycle, J. Geophys. Res., 83, 3369-3376, 1978.

Sibson, R. H., Fault Zone Models, heat flow, and the depth distribution of earthquakes in the continential crust of the United States, Bull. Seism. Soc. Am. 72, 151-163, 1982.

Sieh, K.E., Lateral offsets and revised dates of large prehistoric earthquakes at Pallet Creek, Southern California, J. Geophys. Res., 89, 7641-7670, 1984.

Sieh, K. E. and R. H. Jahns, Holocene activity of the San Andreas fault at Wallace Creek, California, Bull. Geol. Soc. Amer., 95, 883-896, 1984.

Stacey, F. D., Physics of the Earth, 2nd ed., John Wiley, New York, 1977.

Stuart, W. D., Instability model for recurring large and great earthquakes in Southern California, Pure and Appl. Geophys., 122, 793-811, 1984/85.

Stuart, W. D. and G. M. Mavko, Earthquake instability on a strike-slip fault, J. Geophys. Res., 84, 2153-2160, 1979.

Tada, H., P. C. Paris and G. R. Irwin, The Stress Analysis of Cracks Handbook, Del Research Corp., Hellertown, PA, 1973.

Thatcher, W., Strain accumulation and release mechanism of the 1906 San Francisco earthquake, J. of Geophys. Res., 80: 4862-4872, 1975.

Thatcher, W., Systematic inversion of geodetic data in central California, J. Geophys. Res., 84, 2283-95, 1979.

Thatcher, W., Nonlinear strain build-up and the earthquake cycle on the San Andreas Fault, J. Geophys. Res., 88, 5893-5902, 1983.

Thatcher, W., The earthquake deformation cycle at the Nankai Trough, Southwest Japan, J. Geophys. Res., 89, 3087-3101, 1984.

Thatcher, W., T. Matsuda, T. Kato and J. B. Rundle, Lithospheric loading by the 1896 Riku-u earthquake, northern Japan: implications for plate flexure and asthenospheric rheology, J. Geophys. Res., 85, 6429-6439, 1980.

Thatcher, W. and J. B. Rundle, A viscoelastic coupling model for the cyclic deformation due to periodically repeated earthquake at subduction zones, J. Geophys. Res., 89: 7673-7640, 1984.

Thatcher, W. and J. B. Rundle, A model for the earthquake cycle in underthrust zones, J. Geophys. Res., 84: 5540-5556, 1979.

Tse, S. T. and J. R. Rice, Crustal earthquake instability in relation to the depth variation of frictional slip properties, J. Geophys. Res., 91, 9452-9472, 1986.

Tse, S. T., R. Dmowska and J. R. Rice, Stressing of locked patches along a creeping fault, Bull. Seismol. Soc. Amer. 75, 3,709-736, 1985.

Turcotte, D. L. and D. A. Spence, An analysis of strain accumulation on a strike-slip fault, J. Geophys. Res., 79, 4407-4412, 1974.

Turcotte, D. L., J. Y. Liu and F. H. Kulhawy, The role of an intracrustal asthenosphere on the behavior of major strike-slip faults, J. Geophys. Res., 89: 5801-5816, 1984.

Walcott, R. I., Structure of the earth from glacio-isostatic rebound, Annu. Rev. Earth Planet. Sci., 1, 15-37, 1973.

Weldon, R. J., Implications of the age and distribution of the late Cenozoic stratigraphy in Cajon Pass, Southern california, in San Andreas Fault-Cajon Pass to Wrightwood, eds. R. L. Hester and D. E. Halliger, Pacific Section A.A.P.G., Guidebook 55, 9-16, 1984.

Table 1: Calculated and Observed Strain Rate in the Palmdale Area

	$\bar{y}$	$(\Delta y)_{rms}$	$\dot{\gamma}$ (a)	$\dot{\gamma}$ (b)	$\dot{\gamma}$(c)	$\dot{\gamma}$ (King & Savage, 1984)
+Palmdale (1971-82)	-0.3	3.6	0.42	0.41	0.38	0.37 ± 0.02
+S.A. Region (1973-83)	4.1	10.4	0.37	0.38	0.33	0.34 ± 0.01
+Tehachapi (1973-83)	17.0	20.2	0.29	0.31	0.25	0.21 ± 0.01
Los Padres	-19.7	19.7	0.27	0.29	0.23	0.21 ± 0.02 (McGarr et al., 1982)
+Sub Garlock (1973-83; called Garlock region)	31.0	21.1	0.21	0.23	0.18	0.17 ± 0.02

+ subdivision of Tehachapi net

$\dot{\gamma}$ in (μstrain/yr) and $\bar{y}$, $(\Delta y)_{rms}$ in km, positive to the NE. All calculations made for $t = 123$ yr, $T_{cy} = 160$ yr and (a) $V_{pl} = 35$ mm/yr, $L = 9$ km, $H = 22.5$ km, $t_r = 12$ yr; (b) $V_{pl} = 35$ mm/yr, $L = 11$ km, $H = 20$ km, $t_r = 14$ yr; (c) $V_{pl} = 32$ mm/yr, $L = 9$ km, $H = 25$ km, $t_r = 12$ yr.

Figure Captions

Figure 1: (a) Elastic lithosphere coupled to a viscoelastic asthenosphere driven by deep mantle movement. The shaded area indicates the shear zone sliding at constant resistive shear stress below the locked brittle zone. (b) A cross-sectional view of the lithosphere at the plate boundary, modelled as an edge cracked strip in anti-plane strain.

Figure 2: Step movements at plate boundary decomposed into steady motion and a time periodic sawtooth motion, with cycle time T_{cy}.

Figure 3: Surface shear strain rate $\dot{\gamma}_s/(V_{pl}/H)$ as a function of distance from the fault, at various fractions (0.0, 0.1, 0.2, 0.3, 0.4, 0.6, 0.8, 1.0) of an earthquake cycle T_{cy}. These figures are based on $T_{cy} = 160$ yr., $t_r = 12$ yr, and with contrasting locked depths of (a) $L = H$ and (b) $L = 0.3H$. Note that in case (b), where shear slip occurs at depth, the shear strain rate is much more localized at the plate boundary, as is particularly evident during later parts of the earthquake cycle.

Figure 4: Displacement of shear crack wall below locked zone as a function of depth, at various fractions of cycle time. Same parameters as for Figure 3b.

Figure 5: Map of California with locations mentioned in this paper. SC - Shelter Cove; PA - Pt. Arena; FR - Ft. Ross; PR - Pt. Reyes; SF - San Francisco; CP - Carrizo Plain; MD - Mojave Desert; PD - Palmdale; CV - Coachella Valley. (After Allen, 1968; Thatcher, 1983).

Figure 6: Shear strain rate decay with time in an earthquake cycle. The data points with error bars are from Thatcher (1983). The solid circles are from northern California along the 1906 rupture zone of the San Andreas fault. The open circles are from Southern California along the 1857 rupture zone. Curve fits are based on model with indicated parametric values.

Figure 7: Displacement rate profiles, calculated for the parameters indicated.

Figure 8: Geodetic networks in the Palmdale area (after King and Savage, 1984).

Figure 9: Comparisons of theoretically predicted displacement rate profiles to geodetic data from King and Savage (1984). Stations, in order of increasing y, are: Mt. Pinos, Frazier, Sawmill, Tejon 41, Tecuya, Police, Thumb, Wheeler 2, Diorite, Gneiss and Tejon 32.

Figure 10: Geodetic networks in the Point Reyes - Santa Rosa - Napa area (after Prescott and Yu, 1986).

Figure 11: Comparisons of theorectically predicted displacement rate profiles to geodetic data from Prescott and Yu (1986), with error ranges indicated. Circle symbols are data from Pt. Reyes, Santa Rosa and Napa networks. Triangle symbols are from Geyser network further north. The two data points at approximately -20 km and -40 km are associated with the Pt. Reyes Head and Farallon Islands markers.

Figure 12: Geodetic networks in the Coachella Valley - Salton Sea area (after Savage, 1983).

Figure 13: Comparisons of theoretically predicted displacement rate profiles to geodetic data. Data from Savage (1983). Circle symbols are data to the NW of the San Andreas fault. Triangle symbols are data to the SW of San Andreas fault.

Figure B1 Base driven model of lithosphere plates loaded by uniform velocity $V_{pl}/2$ at $y>0$ and $-V_{pl}/2$ at $y<0$.

Figure B2 Comparison of surface displacement rate profiles for base driven model between exact (eqn. B3) and approximate (eqn. B6 and B7) solutions, for (a) $L = 0.25H$ (b) $L = 0.5$ H and (c) $L = 0.75H$.

Figure B3 Comparison of surface strain rate profiles for based driven model between exact (eqn. B5) and approximate (eqn. B8) solutions, for (a) $L = 0.25$ H, (b) $L= 0.5$ H and (c) $L = 0.75$ H.

Figure B4	Ratio of surface strain rate at fault trace between exact and approximate solution, as a function of locked zone depth.
Figure B5	Loading rate distributions on base of edge cracked strip, for base driven model of figure B1 and for viscoelastically coupled model developed in main text.

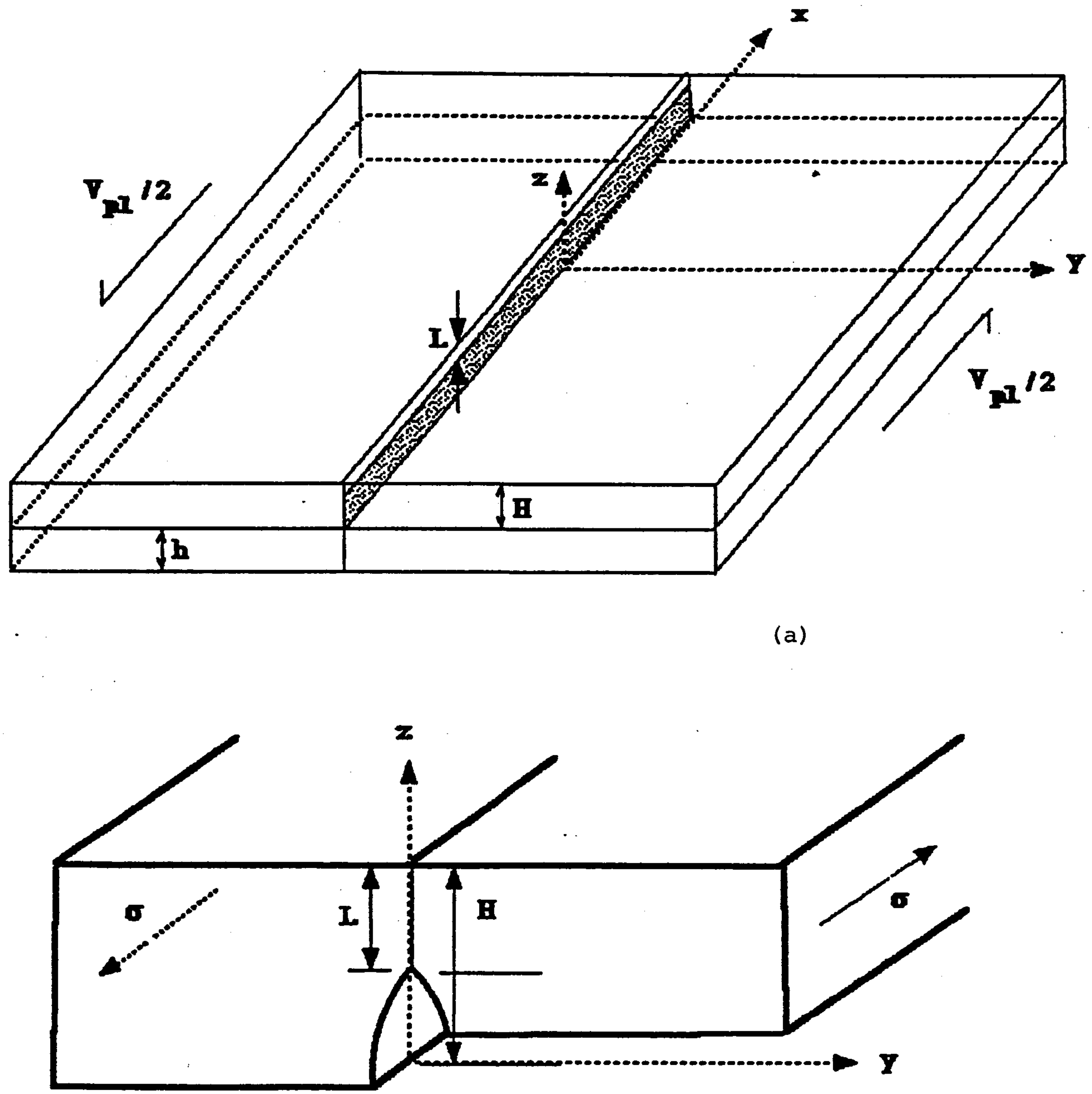

(a)

(b)

Fig. 1

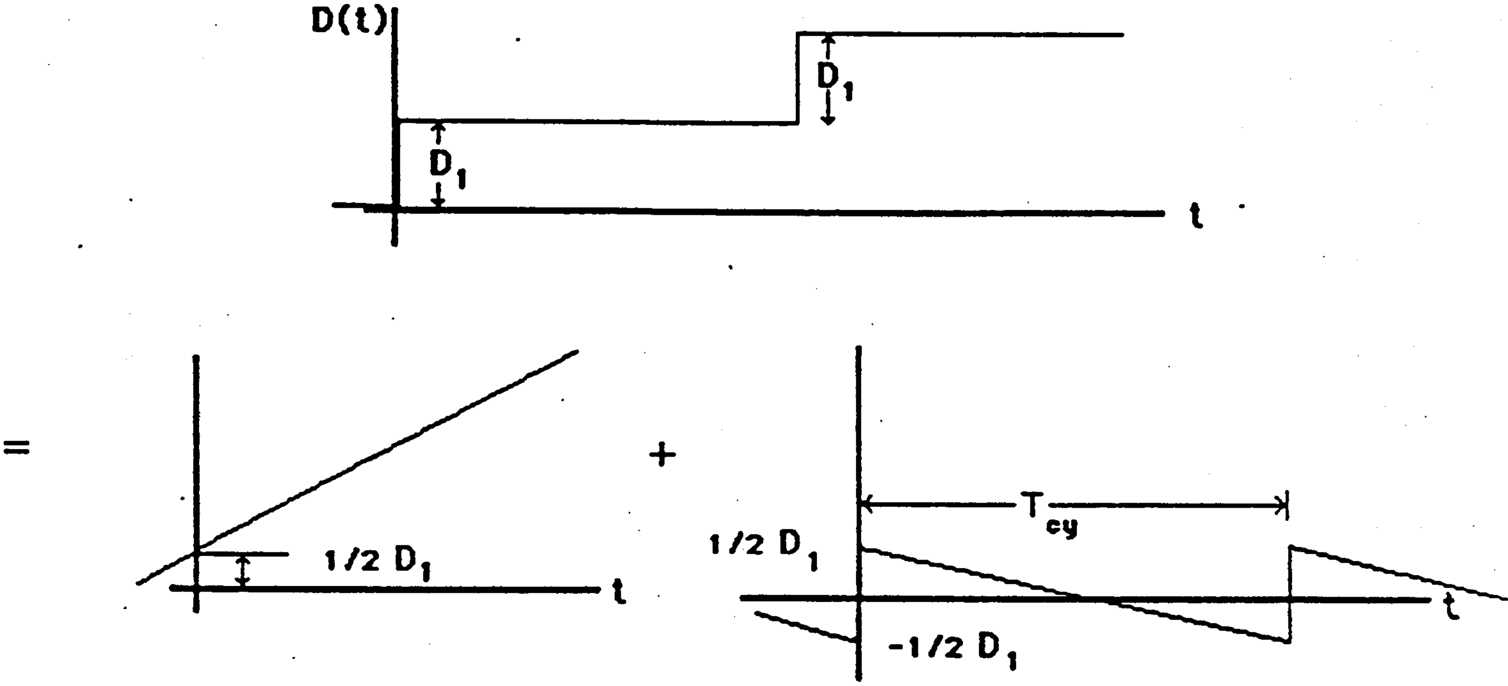

steady motion

periodic sawtooth

Fig. 2

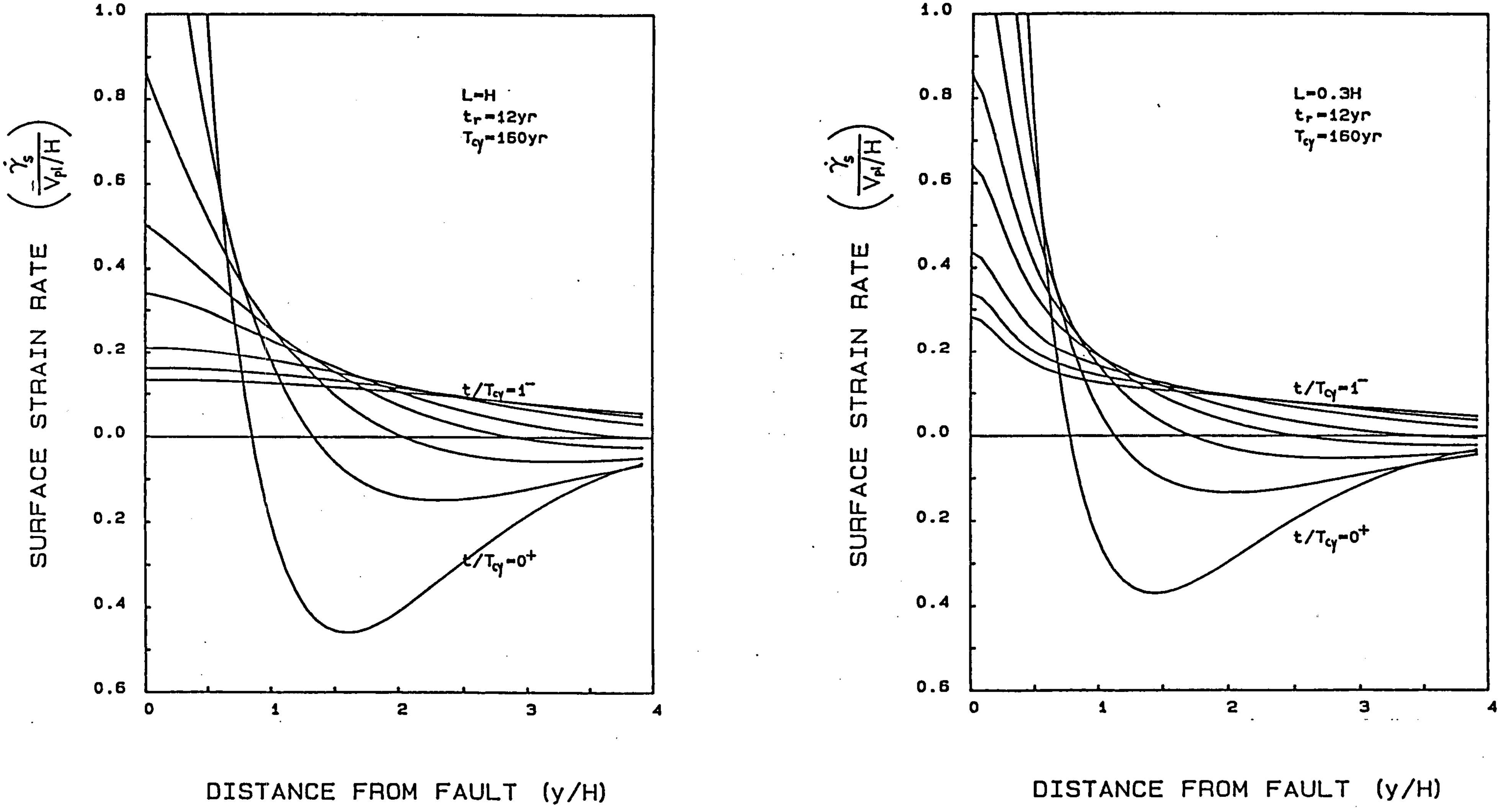
1.0
0.8
0.6
0.4
0.2
0.0
0.2
0.4
0.6
SURFACE STRAIN RATE $\left(\frac{\dot{\gamma}_s}{V_{pl}/H}\right)$
0
1
2
3
4
DISTANCE FROM FAULT (y/H)
L=H
t_r=12yr
T_{cy}=160yr
$t/T_{cy}=1^-$
$t/T_{cy}=0^+$
L=0.3H
t_r=12yr
T_{cy}=160yr

(a)

(b)

Fig. 3

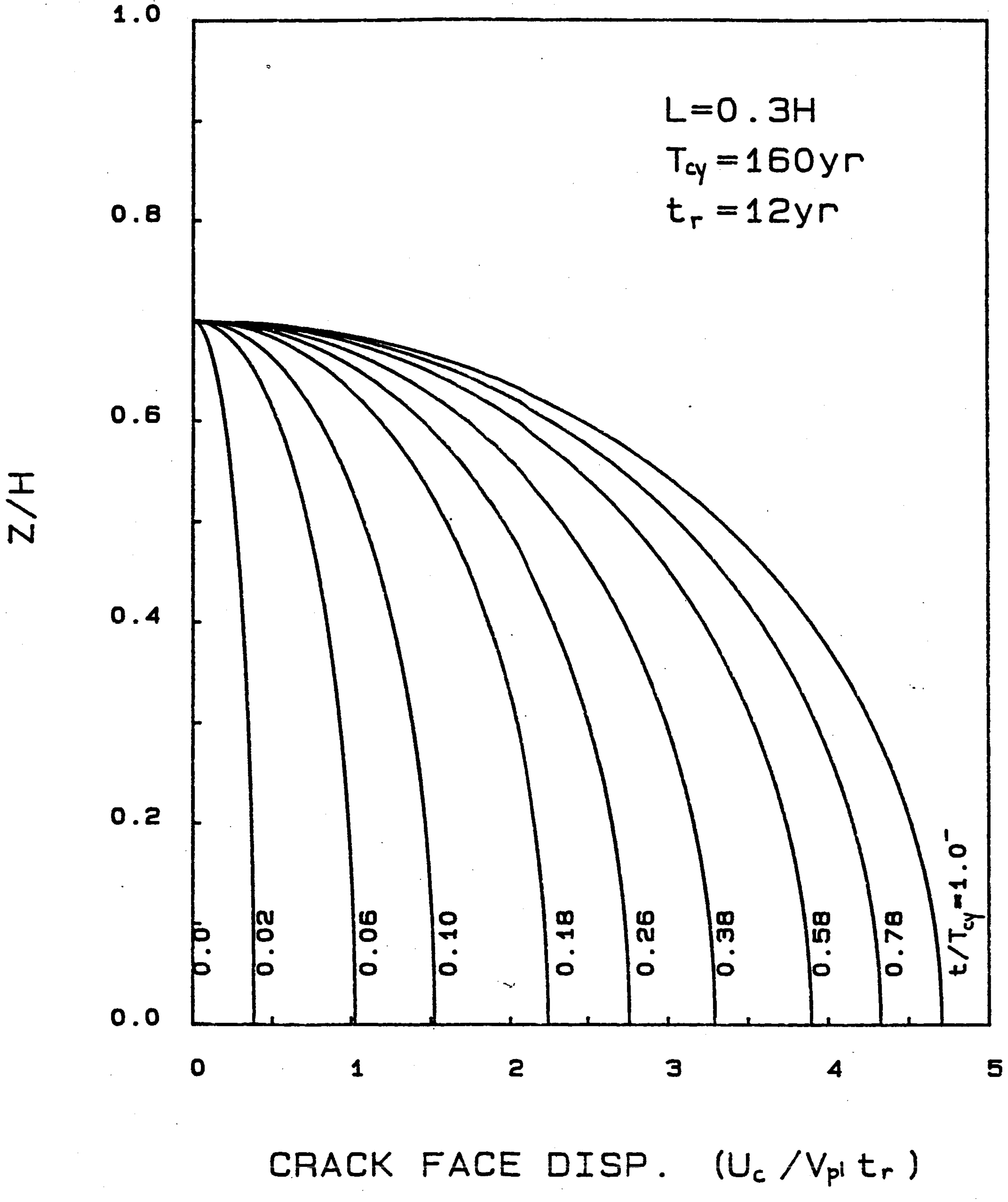
1.0
0.8
0.6
0.4
0.2
0.0
Z/H
L=0.3H
T_{cy}=160yr
t_r=12yr
0.0
0.02
0.06
0.10
0.18
0.26
0.38
0.58
0.78
t/T_{cy}=1.0
0
1
2
3
4
5
CRACK FACE DISP. ($U_c/V_{pl}t_r$)

Fig. 4

ORIGINAL PAGE IS
OF POOR QUALITY

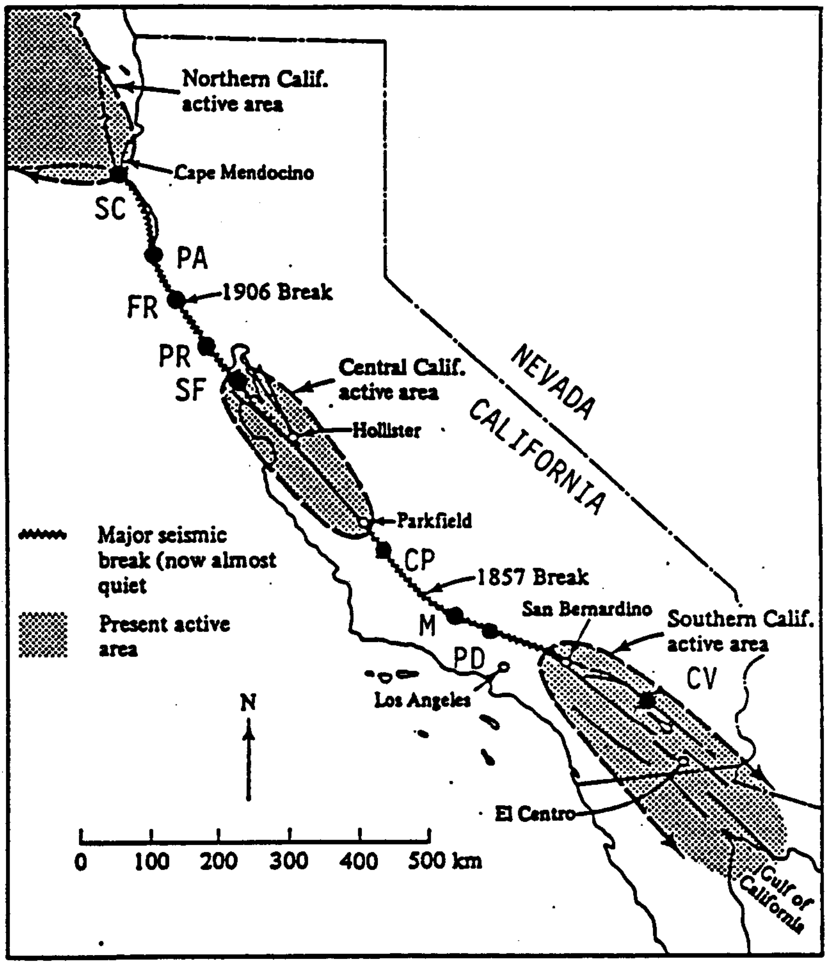

Fig. 5

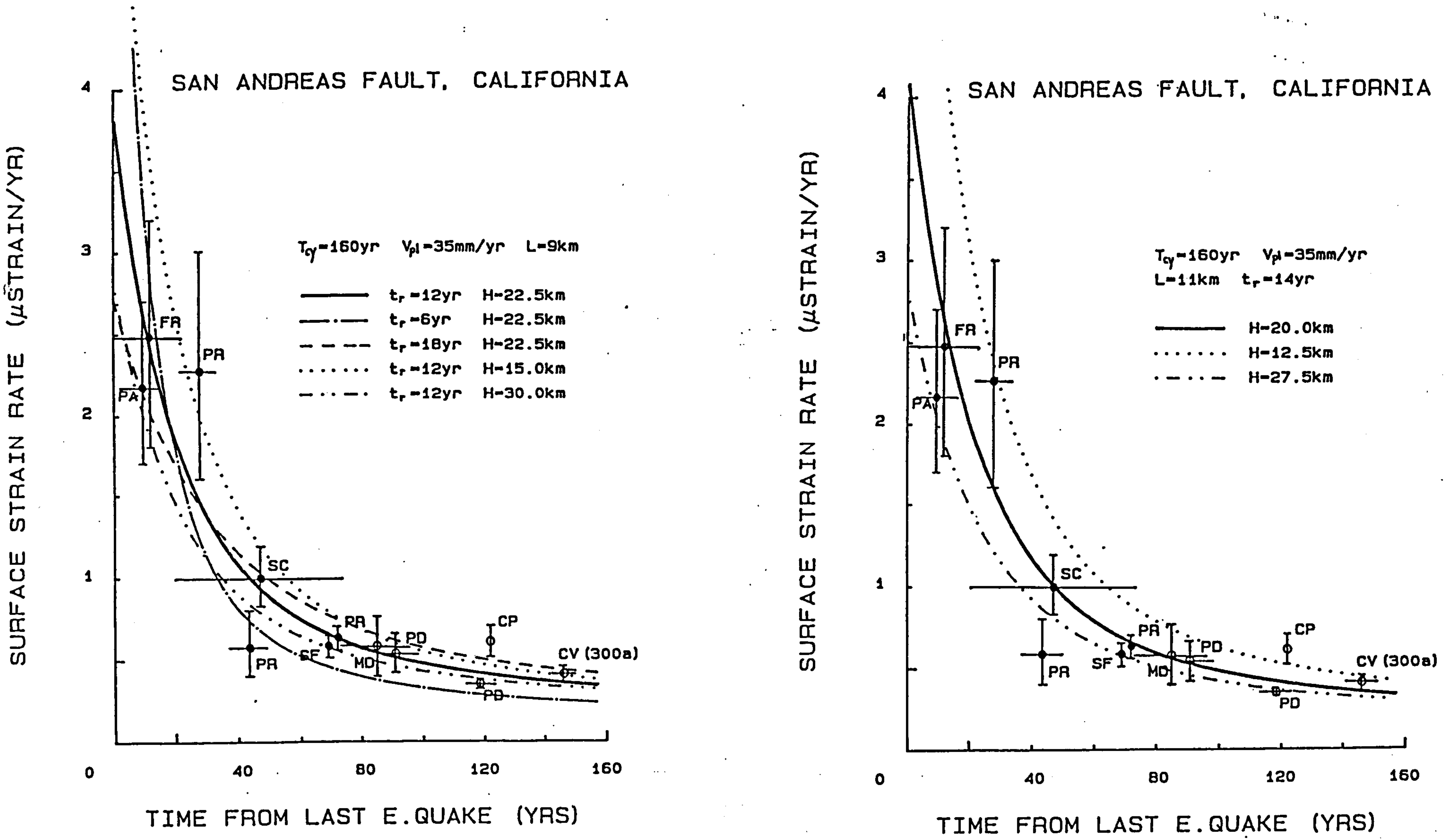
SAN ANDREAS FAULT, CALIFORNIA
T_{cy}=160yr V_{pl}=35mm/yr L=9km
t_r=12yr H=22.5km
t_r=6yr H=22.5km
t_r=18yr H=22.5km
t_r=12yr H=15.0km
t_r=12yr H=30.0km
FR
PR
PA
SC
PR
SF
MD
PD
CP
PD
CV (300a)
SURFACE STRAIN RATE (μSTRAIN/YR)
TIME FROM LAST E.QUAKE (YRS)
0
40
80
120
160
1
2
3
4
SAN ANDREAS FAULT, CALIFORNIA
T_{cy}=160yr V_{pl}=35mm/yr
L=11km t_r=14yr
H=20.0km
H=12.5km
H=27.5km
FR
PR
PA
SC
PR
SF
MD
PD
CP
PD
CV (300a)
SURFACE STRAIN RATE (μSTRAIN/YR)
TIME FROM LAST E.QUAKE (YRS)
0
40
80
120
160
1
2
3
4

(a)

(b)

Fig. 6

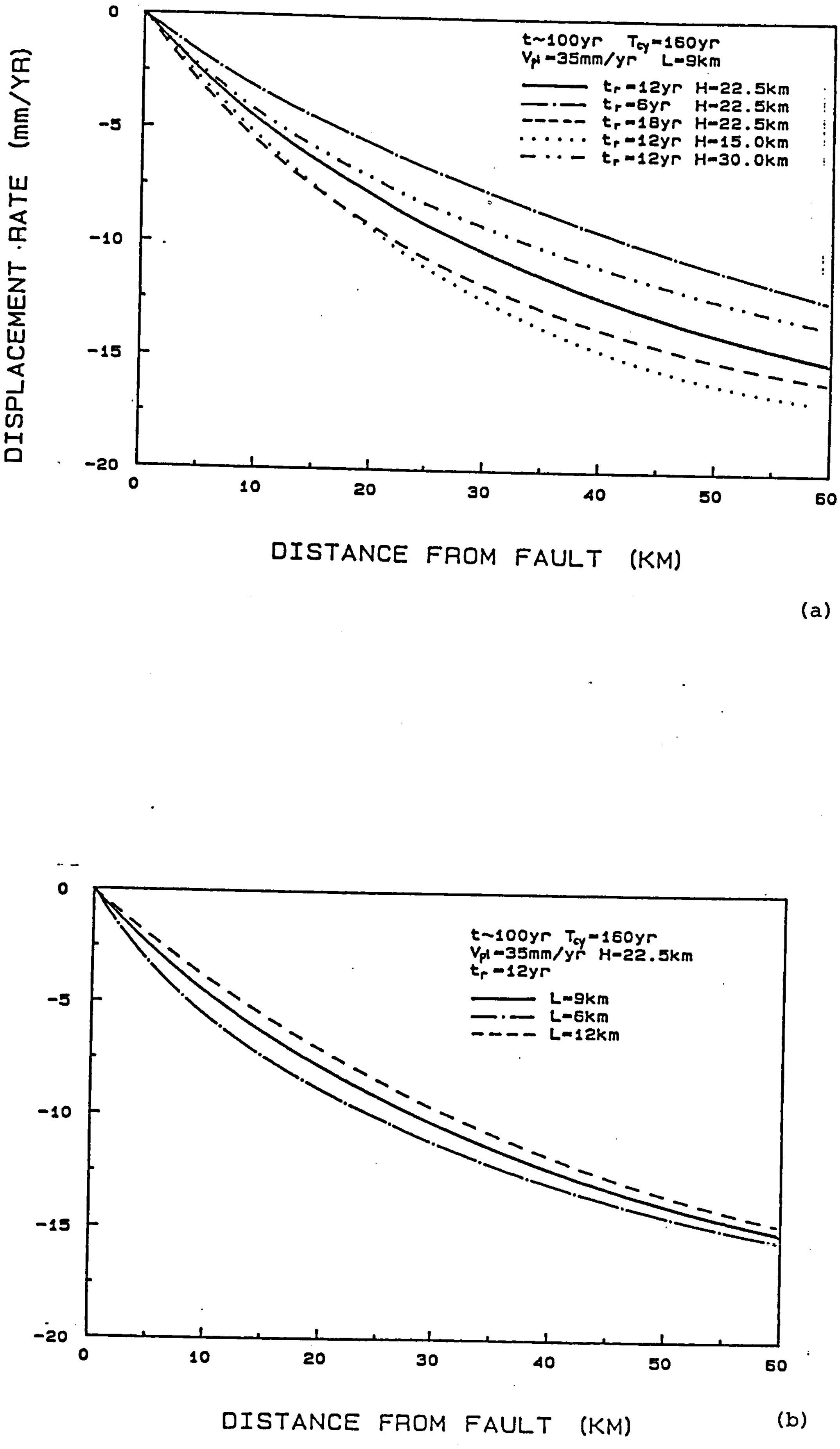
0
-5
-10
-15
-20
DISPLACEMENT RATE (mm/YR)
0
10
20
30
40
50
60
DISTANCE FROM FAULT (KM)
t~100yr T_cy=160yr
V_pl=35mm/yr L=9km
t_r=12yr H=22.5km
t_r=6yr H=22.5km
t_r=18yr H=22.5km
t_r=12yr H=15.0km
t_r=12yr H=30.0km
(a)
0
-5
-10
-15
-20
DISPLACEMENT RATE (mm/YR)
0
10
20
30
40
50
60
DISTANCE FROM FAULT (KM)
t~100yr T_cy=160yr
V_pl=35mm/yr H=22.5km
t_r=12yr
L=9km
L=6km
L=12km
(b)

Fig. 7

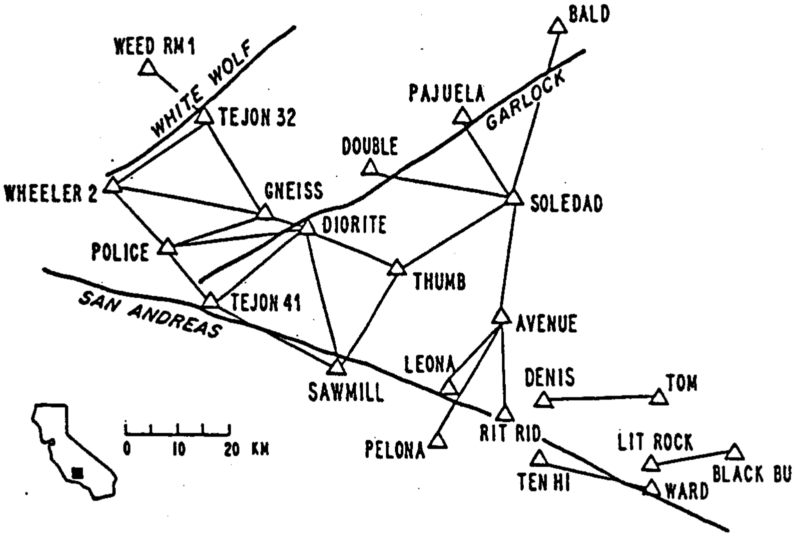
BALD
WEED RM1
WHITE WOLF
PAJUELA
GARLOCK
TEJON 32
DOUBLE
WHEELER 2
GNEISS
SOLEDAD
DIORITE
POLICE
THUMB
TEJON 41
SAN ANDREAS
AVENUE
LEONA
DENIS
TOM
SAWMILL
RIT RID
LIT ROCK
PELONA
BLACK BU
TEN HI
WARD
0
10
20 KM

Fig. 8

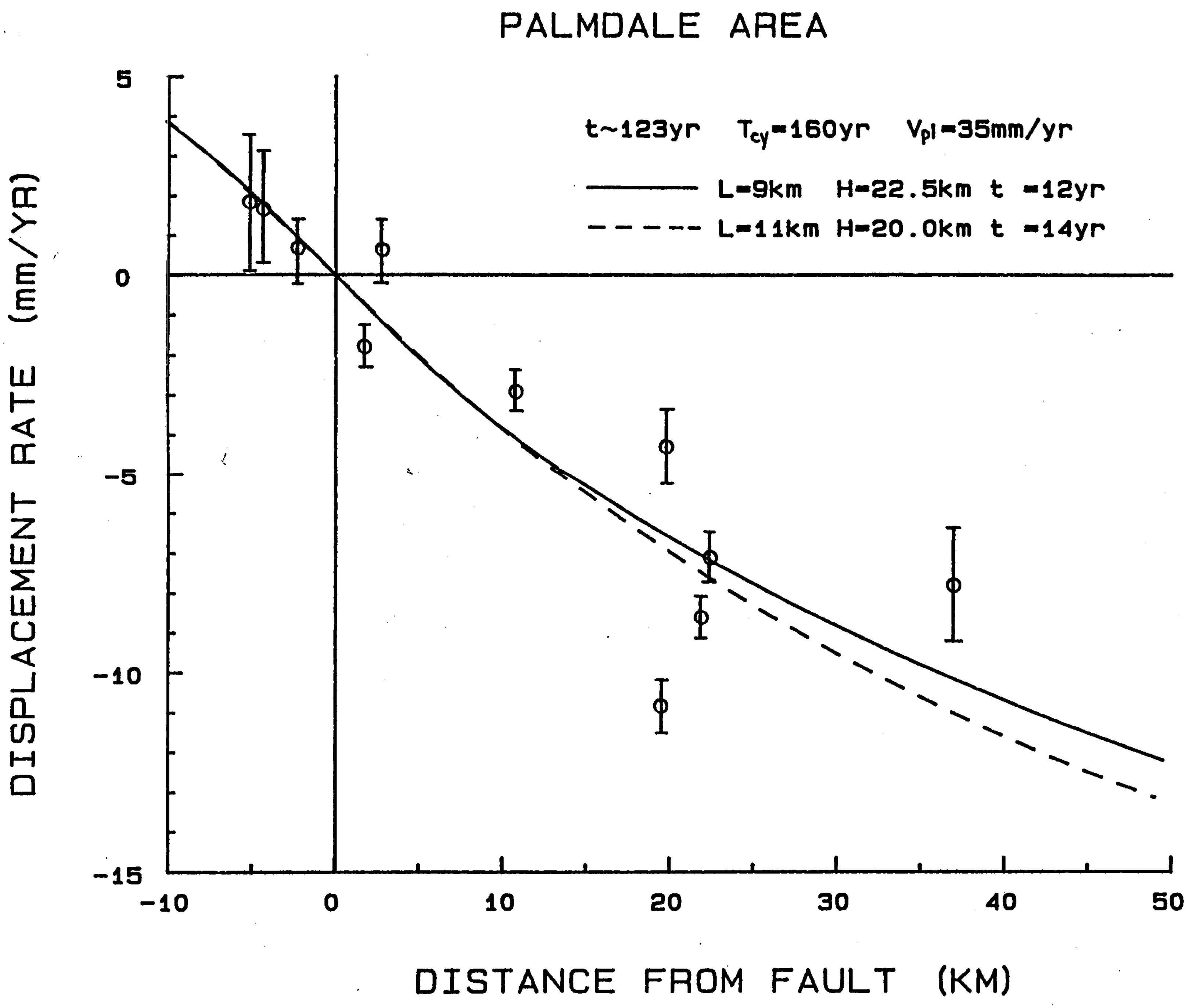
PALMDALE AREA
t~123yr T$_{cy}$=160yr V$_{pl}$=35mm/yr
L=9km H=22.5km t =12yr
L=11km H=20.0km t =14yr
DISPLACEMENT RATE (mm/YR)
5
0
-5
-10
-15
-10
0
10
20
30
40
50
DISTANCE FROM FAULT (KM)

Fig. 9

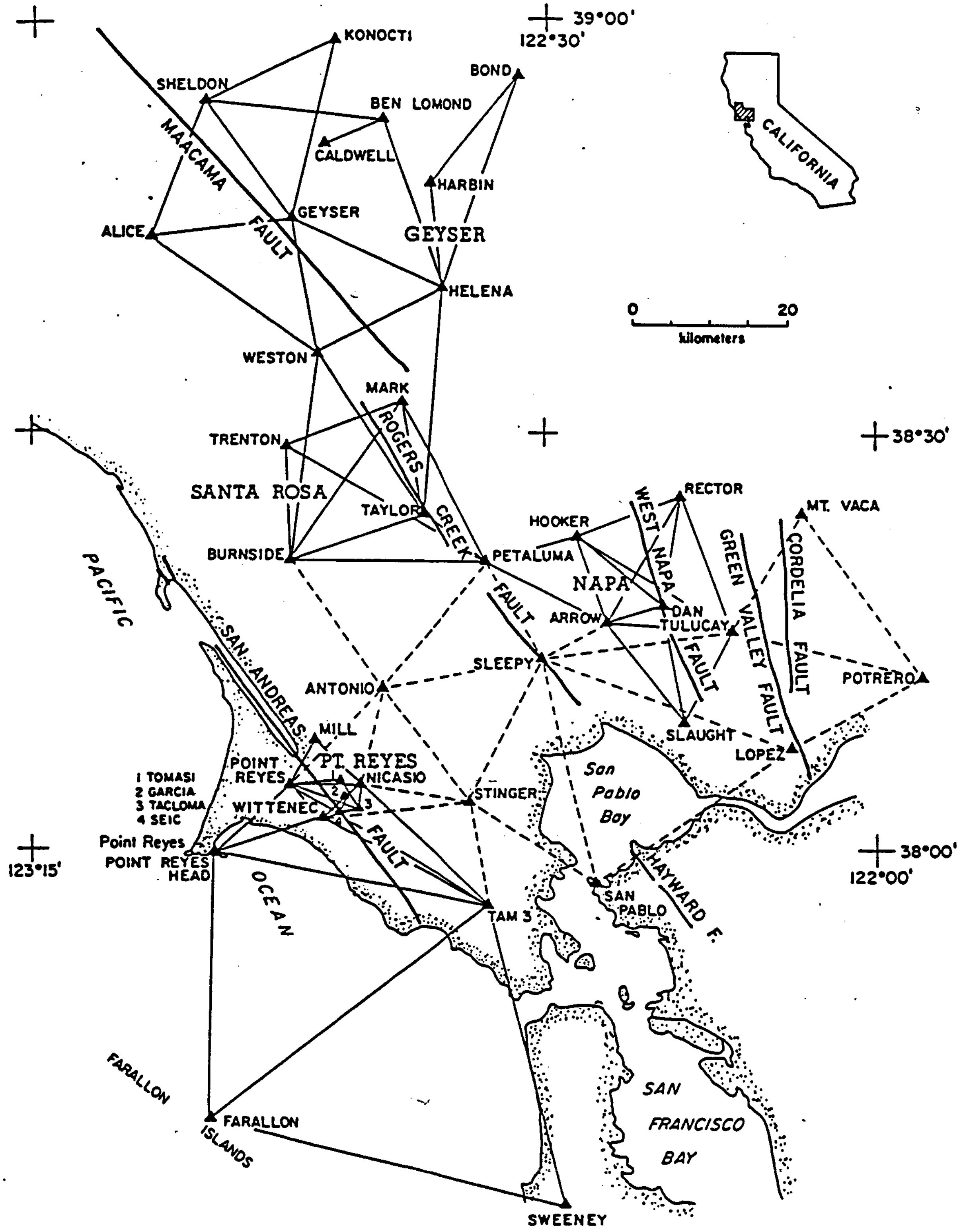
39°00'
122°30'
KONOCTI
SHELDON
BOND
BEN LOMOND
CALDWELL
HARBIN
MAACAMA FAULT
CALIFORNIA
GEYSER
ALICE
GEYSER
HELENA
0
20
kilometers
WESTON
MARK
TRENTON
ROGERS CREEK FAULT
38°30'
SANTA ROSA
TAYLOR
RECTOR
HOOKER
WEST NAPA FAULT
MT. VACA
GREEN VALLEY FAULT
CORDELIA FAULT
BURNSIDE
PETALUMA
PACIFIC
NAPA
ARROW
DAN
TULUCAY
SLEEPY
POTRERO
ANTONIO
SAN ANDREAS
SLAUGHT
LOPEZ
MILL
PT. REYES
POINT REYES
NICASIO
1 TOMASI
2 GARCIA
3 TACLOMA
4 SEIC
WITTENEC
STINGER
San Pablo Bay
38°00'
122°00'
Point Reyes
POINT REYES HEAD
123°15'
OCEAN
FAULT
SAN PABLO
HAYWARD F.
TAM 3
SAN FRANCISCO BAY
FARALLON ISLANDS
FARALLON
SWEENEY

Fig. 10

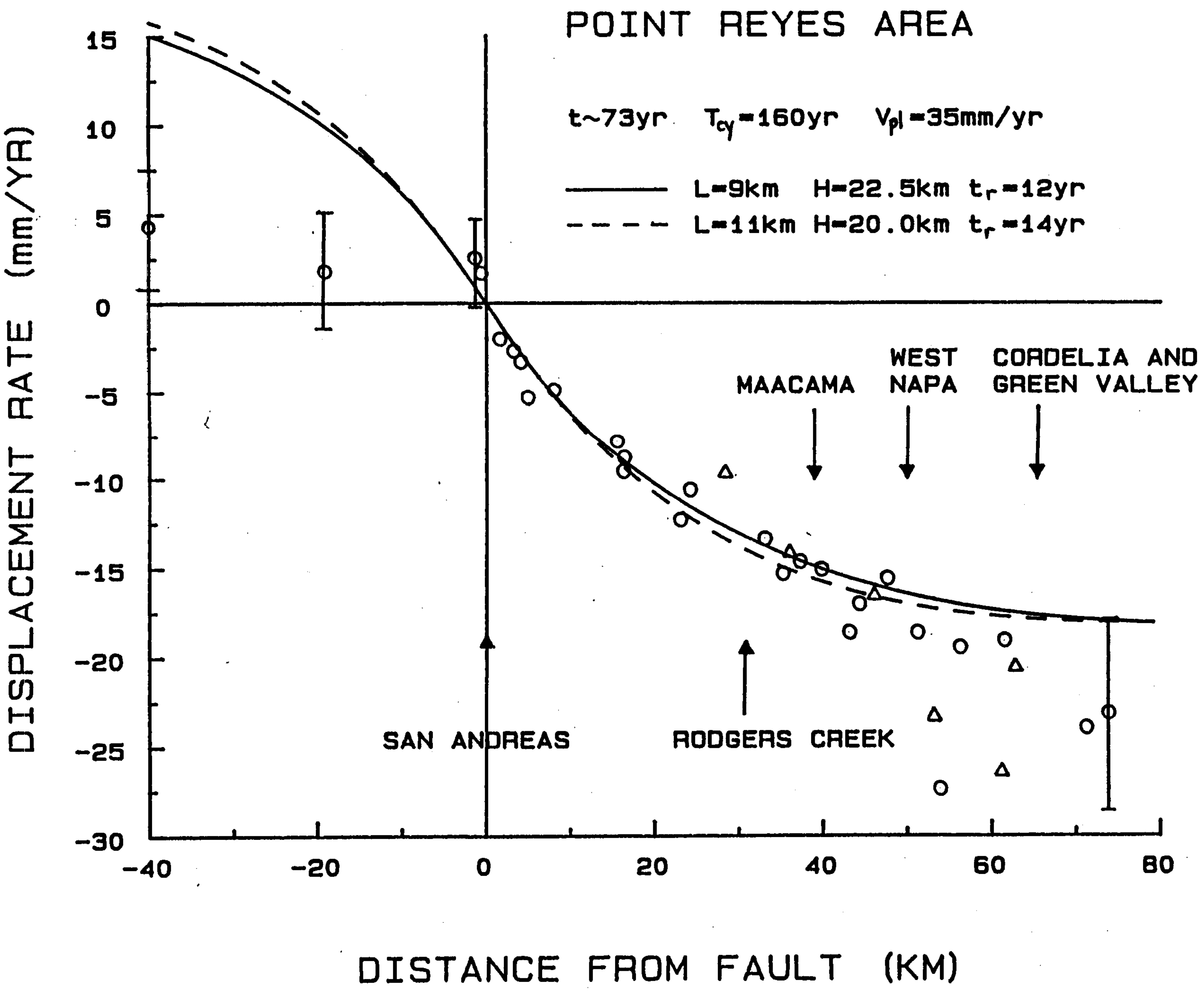

POINT REYES AREA
t~73yr T_{cy}=160yr V_{pl}=35mm/yr
L=9km H=22.5km t_r=12yr
L=11km H=20.0km t_r=14yr
MAACAMA
WEST NAPA
CORDELIA AND GREEN VALLEY
SAN ANDREAS
RODGERS CREEK
DISPLACEMENT RATE (mm/YR)
15
10
5
0
-5
-10
-15
-20
-25
-30
-40
-20
0
20
40
60
80
DISTANCE FROM FAULT (KM)

Fig. 11

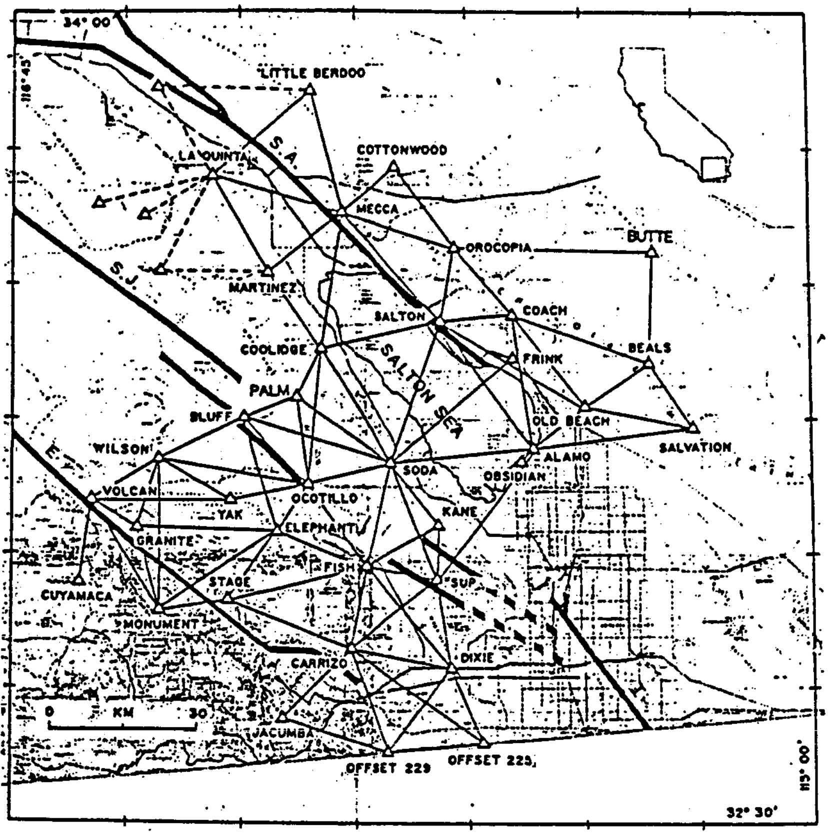
34° 00'
116°45'
LITTLE BERDOO
COTTONWOOD
S.A.
LA QUINTA
MECCA
OROCOPIA
BUTTE
S.J.
MARTINEZ
SALTON
COACH
COOLIDGE
SALTON SEA
FRINK
BEALS
PALM
BLUFF
OLD BEACH
SALVATION
WILSON
ALAMO
SODA
OBSIDIAN
E.
VOLCAN
OCOTILLO
YAK
KANE
ELEPHANT
GRANITE
FISH
STAGE
SUP
CUYAMACA
MONUMENT
CARRIZO
DIXIE
0
KM
30
JACUMBA
OFFSET 229
OFFSET 225
115° 00'
32° 30'

Fig. 12

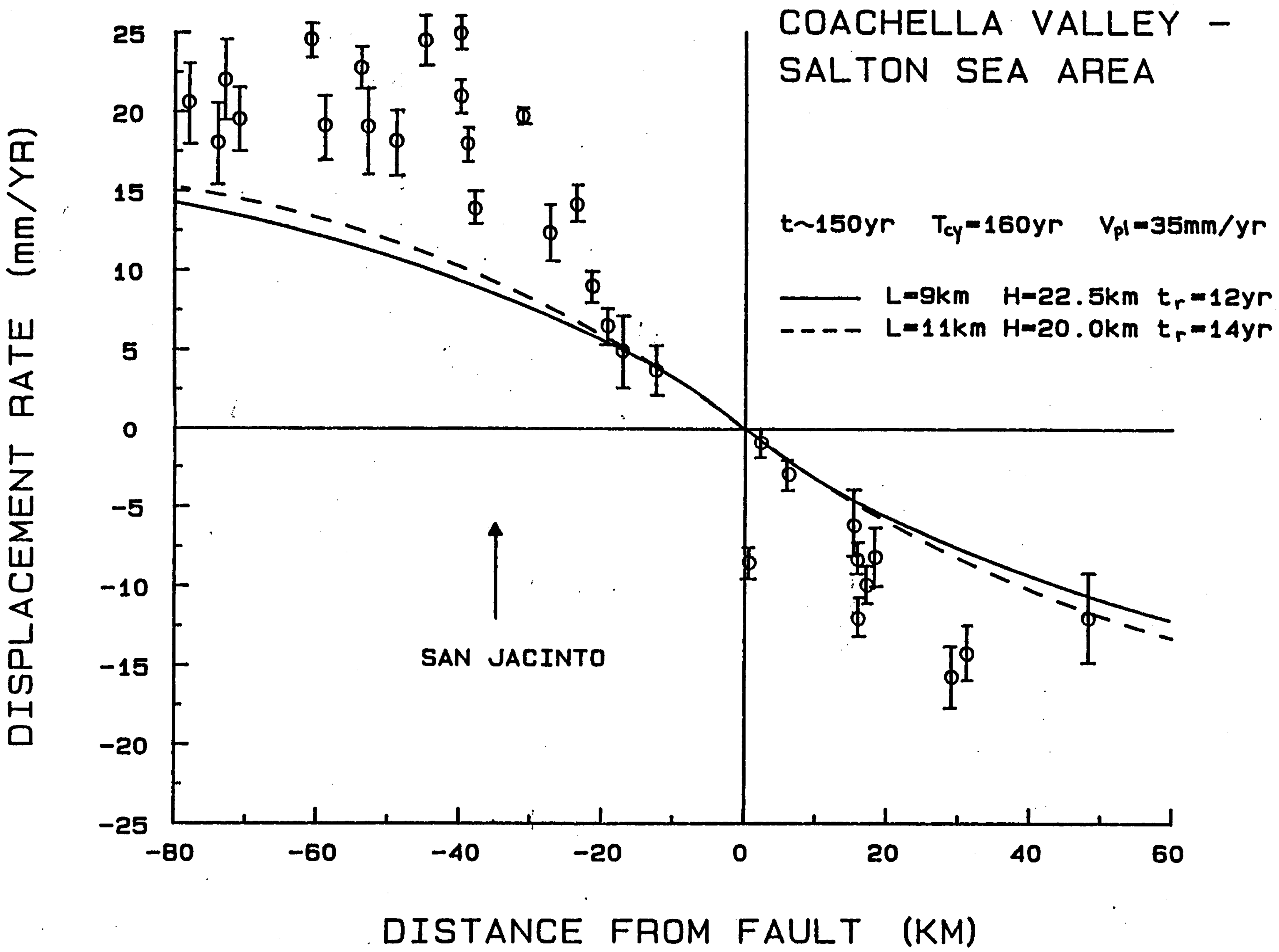
COACHELLA VALLEY –
SALTON SEA AREA
t~150yr T_{cy}=160yr V_{pl}=35mm/yr
L=9km H=22.5km t_r=12yr
L=11km H=20.0km t_r=14yr
SAN JACINTO
DISPLACEMENT RATE (mm/YR)
25
20
15
10
5
0
-5
-10
-15
-20
-25
-80
-60
-40
-20
0
20
40
60
DISTANCE FROM FAULT (KM)

Fig. 13

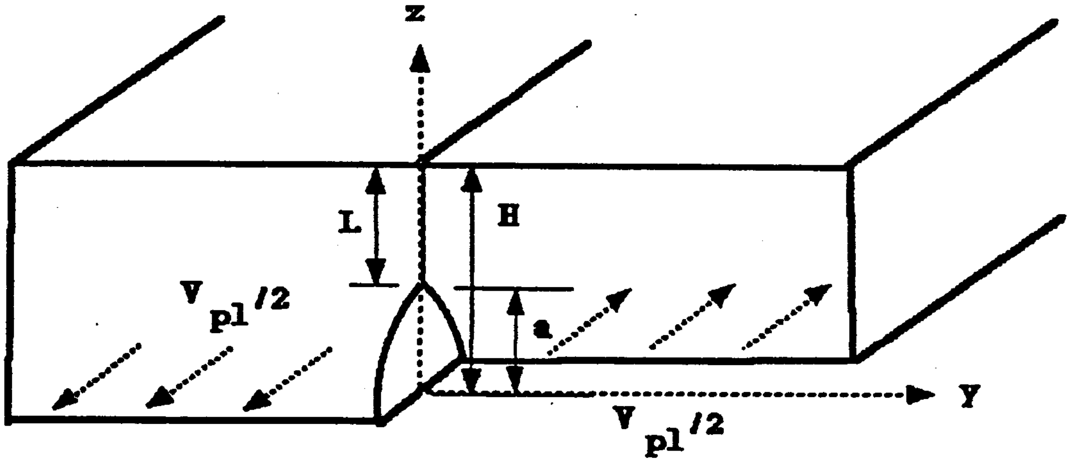

Fig. B1

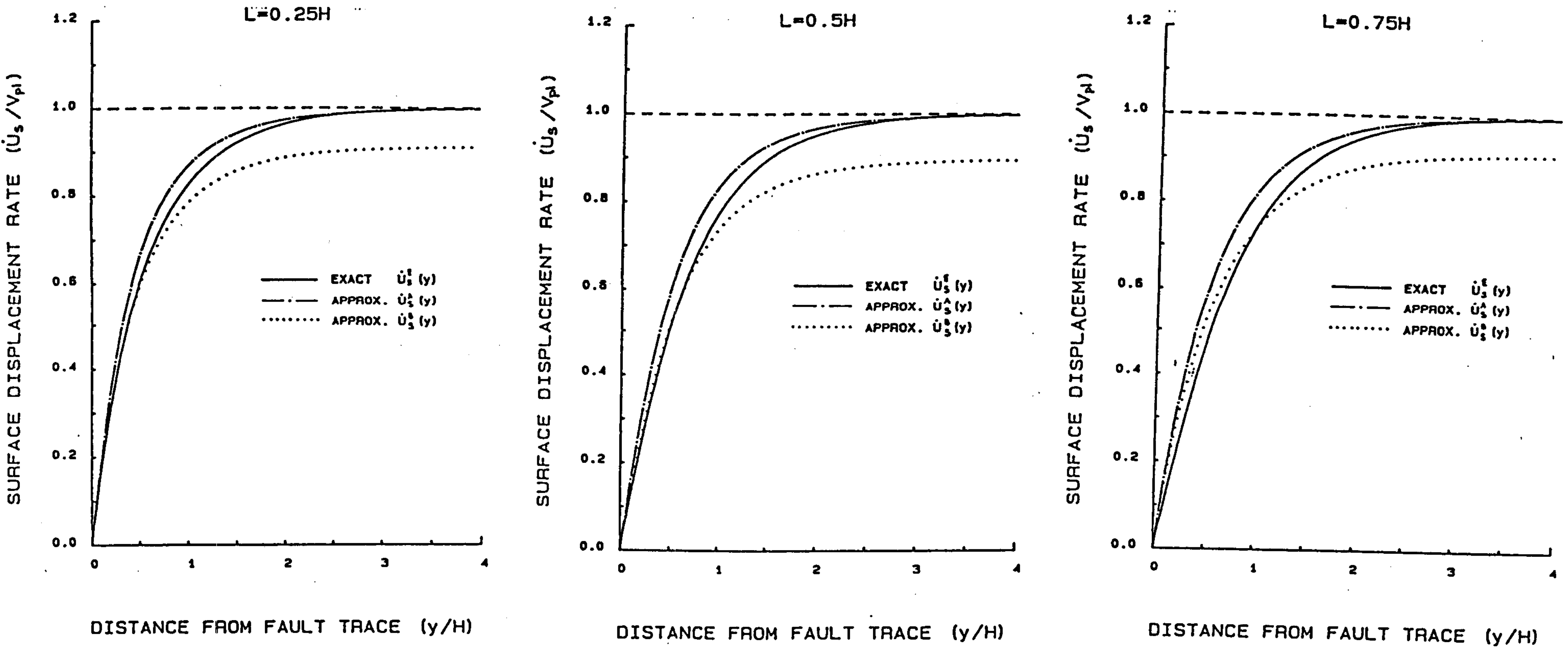
L=0.25H
L=0.5H
L=0.75H
SURFACE DISPLACEMENT RATE $(\dot{U}_s/V_{pl})$
1.2
1.0
0.8
0.6
0.4
0.2
0.0
0
1
2
3
4
DISTANCE FROM FAULT TRACE (y/H)
EXACT $\dot{U}_s^E(y)$
APPROX. $\dot{U}_s^A(y)$
APPROX. $\dot{U}_s^B(y)$

(a)

(b)

(c)

Fig. B2

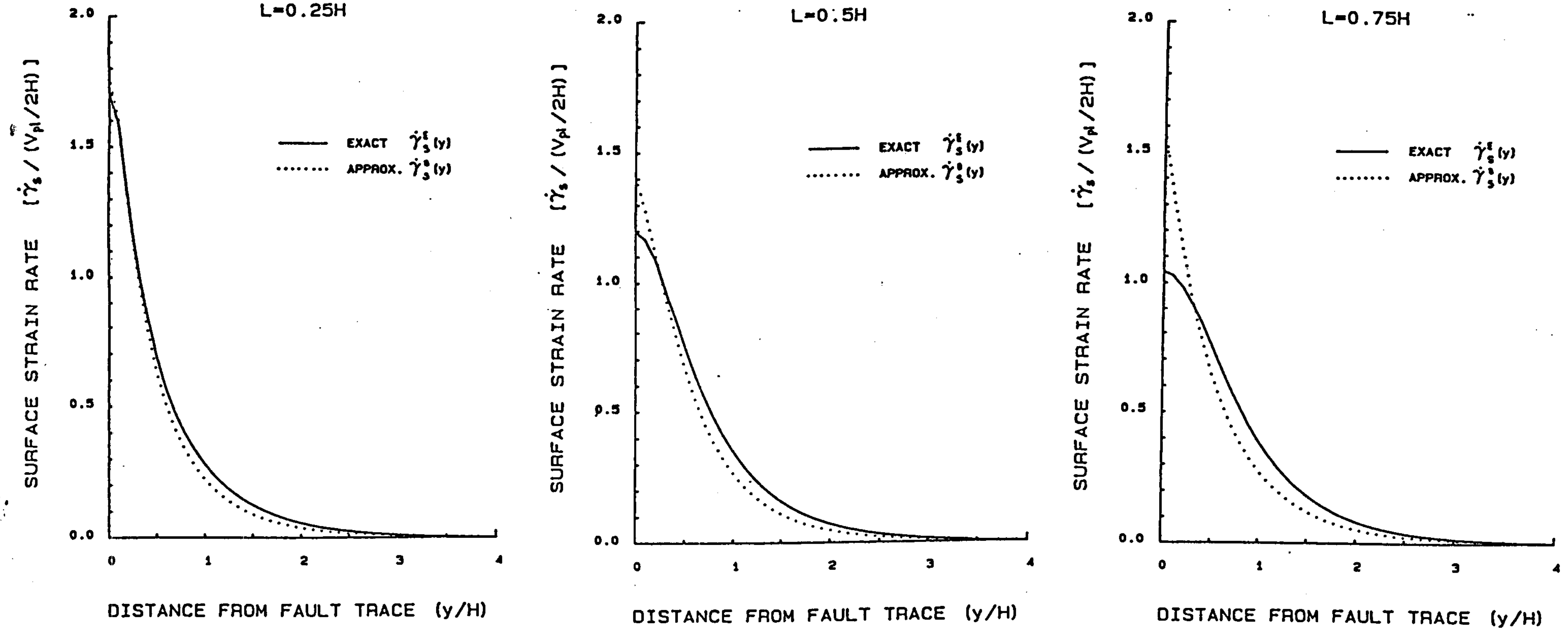
L=0.25H
L=0.5H
L=0.75H
EXACT $\dot{\gamma}_s^E(y)$
APPROX. $\dot{\gamma}_s^a(y)$
SURFACE STRAIN RATE $[\dot{\gamma}_s / (V_{pl}/2H)]$
DISTANCE FROM FAULT TRACE (y/H)
2.0
1.5
1.0
0.5
0.0
0
1
2
3
4

(a)

(b)

(c)

Fig. B3

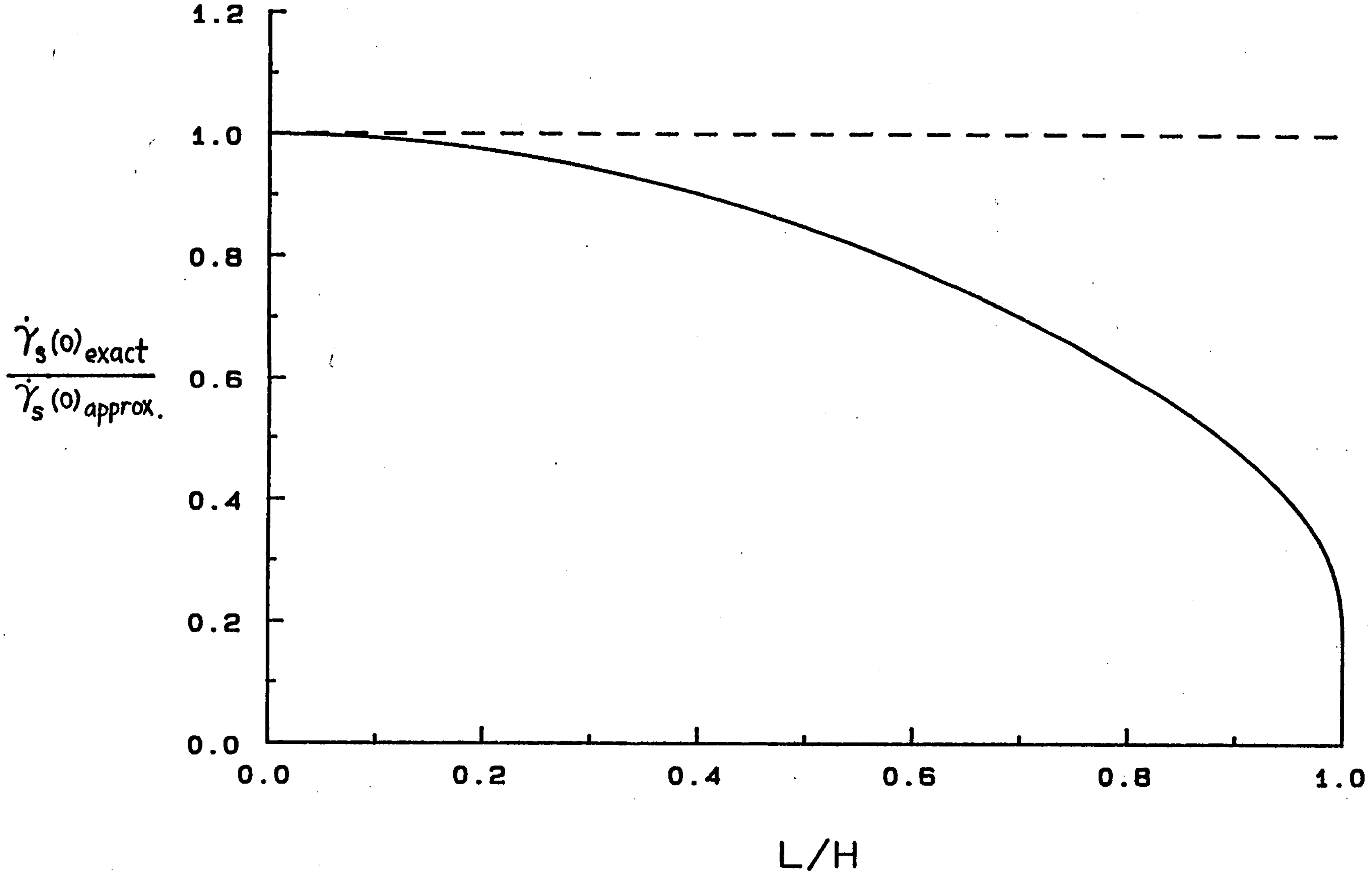
$\frac{\dot{\gamma}_s(0)_{exact}}{\dot{\gamma}_s(0)_{approx.}}$
1.2
1.0
0.8
0.6
0.4
0.2
0.0
0.0
0.2
0.4
0.6
0.8
1.0
L/H

Fig. B4

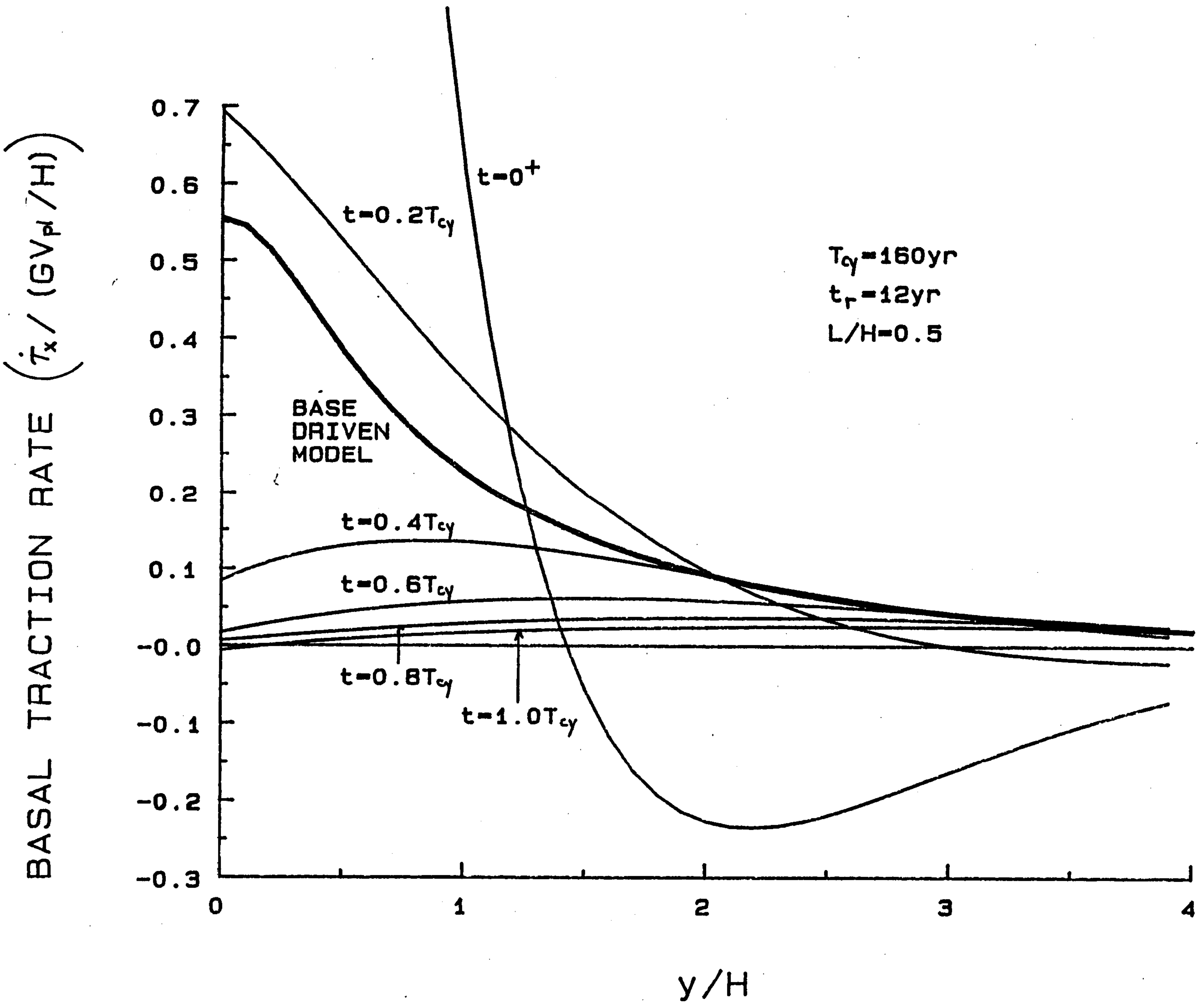
BASAL TRACTION RATE $\left(\dot{\tau}_x / (GV_{pl}/H)\right)$
0.7
0.6
0.5
0.4
0.3
0.2
0.1
-0.0
-0.1
-0.2
-0.3
0
1
2
3
4
y/H
t=0+
t=0.2Tcy
BASE DRIVEN MODEL
t=0.4Tcy
t=0.6Tcy
t=0.8Tcy
t=1.0Tcy
Tcy=160yr
tr=12yr
L/H=0.5

Fig. B5